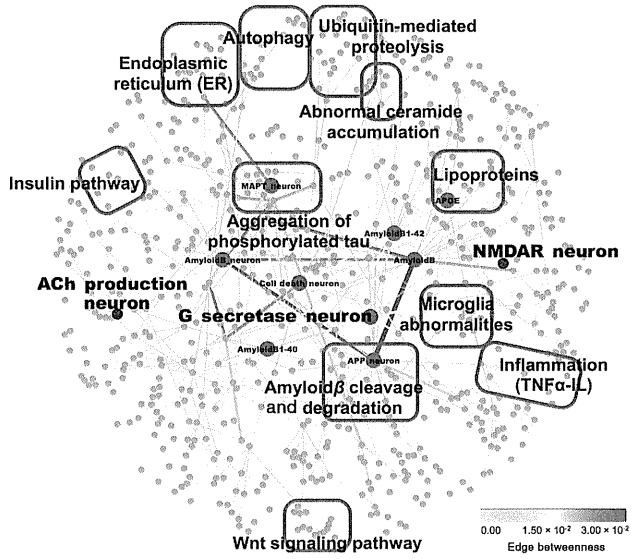

Figure 2 Key molecules in AlzPathway. Overview of AlzPathway in binary-relation notation, and key molecules showing high centrality. The drug targeting a key molecule might be effective but could cause significant side effects due to off-target and/or unintended downstream target effects. ACh, acetylcholine; APOE, apolipoprotein E; APP, amyloid precursor protein; MAPT, microtubule-associated protein τ; NMDAR, *N*-methyl-D-aspartate receptor; TNF, tumor necrosis factor.

(memanatine). They are dementia-suppressing drugs, rather than AD curative drugs. Of note, when mapped in the AlzPathway, no compensatory or major interacting pathway is observed around cholinesterase and the *N*-methyl-D-aspartic acid receptor (Figure 1), implying that these pathways are vulnerable to inhibition without off-target effects. Moreover, both the acetylcholine and *N*-methyl-D-aspartic acid receptors are peripheral molecules (not key molecules) in the AlzPathway (Figure 2). Because these target molecules have low centrality in the AD-signaling network, their inhibitors are predicted to have relatively specific effects without eliciting broader influences on off-target network elements.

CONCLUDING REMARKS

More than 25 drugs have been targeted to the β-amyloid pathway, but none has been successfully marketed for various reasons. The AlzPathway provides an integrated platform of comprehensive AD signaling that may be used to inform the AD drug discovery and development processes. If proven successful, the AlzPathway will serve as a model for pathway-based drug discovery in other diseases.

ACKNOWLEDGMENT

We are grateful for the helpful comments from the editor. This work was supported by a Grant-in-Aid for Scientific Research (22700311) from the Ministry of Education, Culture, Sports, Science and Technology (MEXT) of Japan. This work was also supported by MEXT Tohoku Medical Megabank Project.

CONFLICT OF INTEREST

The authors declared no conflict of interest.

1. Kitano, H. A robustness-based approach to systems-oriented drug design. *Nat. Rev. Drug Discov.* **6**, 202–210 (2007).
2. Ballard, C., Gauthier, S., Corbett, A., Brayne, C., Aarsland, D. & Jones, E. Alzheimer's disease. *Lancet* **377**, 1019–1031 (2011).
3. Mizuno, S. *et al.* AlzPathway: a comprehensive map of signaling pathways of Alzheimer's disease. *BMC Syst. Biol.* **6**, 52 (2012).
4. Funahashi, A., Matsuoka, Y., Jouraku, A., Morohashi, M., Kikuchi, N. & Kitano, H. CellDesigner 3.5: a versatile modeling tool for biochemical networks. *Proc IEEE* **96**, 1254–1265 (2008).
5. Matsuoka, Y., Ghosh, S., Kikuchi, N. & Kitano, H. Payao: a community platform for SBML pathway model curation. *Bioinformatics* **26**, 1381–1383 (2010).

HEPATOLOGY
Official Journal of the American Association for the Study of Liver Diseases

Visualization of Stem Cell Features in Human Hepatocellular Carcinoma Reveals *In Vivo* Significance of Tumor-Host Interaction and Clinical Course

Shunsuke Muramatsu,[1] Shinji Tanaka,[1] Kaoru Mogushi,[2] Rama Adikrisna,[1] Arihiro Aihara,[1] Daisuke Ban,[1] Takanori Ochiai,[1] Takumi Irie,[1] Atsushi Kudo,[1] Noriaki Nakamura,[1] Koh Nakayama,[3] Hiroshi Tanaka,[2] Shoji Yamaoka,[4] and Shigeki Arii[1]

Hepatocellular carcinoma (HCC) is one of the most aggressive malignancies because of recurrence and/or metastasis even after curative resection. Emerging evidence suggests that tumor metastasis and recurrence might be driven by a small subpopulation of stemness cells, so-called cancer stem cells (CSCs). Previous investigations have revealed that glioma and breast CSCs exhibit intrinsically low proteasome activity and that breast CSCs also reportedly contain a lower reactive oxygen species (ROS) level than corresponding nontumorigenic cells. Here we visualized two stem cell features, low proteasome activity and low intracellular ROS, in HCC cells using two-color fluorescence activated cell sorting to isolate cells with stem cell features. These cells were then analyzed for their division behavior in normoxia and hypoxia, expression of stem cell markers, tumorigenicity, metastatic potential, specific gene expression signatures, and their clinical implications. A visualized small subpopulation of HCC cells demonstrated asymmetric divisions. Their remarkable tumorigenicity in nonobese diabetic/severe combined immunodeficient mice suggested the cancer initiation potential of these HCC CSCs. Comprehensive gene expression analysis revealed that chemokine-related genes were up-regulated in the CSCs subpopulation. Our identified HCC CSCs facilitated the migration of macrophages *in vitro* and demonstrated metastatic potential by way of recruitment of macrophages *in vivo*. In patients who undergo curative operation for HCC, the CSC-specific gene signature in the liver microenvironment significantly correlates with recurrence. *Conclusion*: Based on these findings, the stem cell feature monitoring system proposed here is a promising tool to analyze the *in vivo* significance of CSC microenvironments in human HCCs. (HEPATOLOGY 2013;00:000-000)

Hepatocellular carcinoma (HCC) is one of the most common malignancies and the third leading cause of cancer death worldwide.[1] The primary curative treatment for HCC is surgical resection; however, even after curative resection patient prognosis remains poor because of frequent recurrence and/or metastasis.[2,3] Because cancer stem cells (CSCs) possess self-renewal capacity, multilineage potency, and increased tumorigenicity, it has been hypothesized that CSCs exist as a small population within the bulk tumors and play a critical role in cancer progression, metastasis, and recurrence.[4] Various tools have been reported for identification of the CSC population, including the cell surface markers CD44, CD133, CD90, and ESA/EpCAM.[5-8] In addition, specific stemness properties based on stem cell biology of their intracellular activities may be useful in identifying CSCs.[9] For example, one property that may be useful in identifying stemness is 26S proteasome activity, which is involved in a diverse array of biological processes, including cell-cycle progression, DNA repair, apoptosis, and protein quality control.[10] Proteasome activity is significantly activated in cancer cells with proliferating and hypermetabolic activities, but generally suppressed in dormant states of stem cells.[11] Vlashi et al.[12] reported that human glioma and breast CSCs were identical to the subpopulation of cells monitored by green fluorescent protein ZsGreen fused to a degron motif of ornithine decarboxylase (ODC), which accumulated within the cell because of low 26S proteasome activity. Stem cells are also characterized by resistance to oxidative stress (superoxide) according to data obtained using the detoxifier system.[13] Hematopoietic stem cells contain a lower level of reactive oxygen species (ROS) than their mature progeny, and these differences are critical for maintaining stem cell function.[14] Human breast CSCs contain lower ROS levels, especially mitochondrial superoxide, than corresponding nontumorigenic cells.[15] In this study, we visualized two stem cell features, low proteasome activity and low ROS levels, in human HCC cells using the ZsGreen-fused degron sequence of ODC and the mitochondrial superoxide indicator MitoSOX Red, respectively. This monitoring system of stemness is a promising tool to elucidate the mechanism of progression and metastasis of human HCC.

Materials and Methods

Cell Culture. HCC cell lines (Hep3B, SK-Hep1, HuH7, and HLF) were purchased from the American Type Culture Collection (Manassas, VA) and the Human Science Research Resources Bank (Osaka, Japan). HuH7, Hep3B, and SK-Hep1 cells were cultured in log-growth phase in 1640 RPMI medium (Invitrogen, Carlsbad, CA), supplemented with 10% fetal bovine serum (Sigma-Aldrich, St. Louis, MO) and Pen/Strep (Sigma) as antibiotics. HLF cells were cultured in Dulbecco's modified Eagle's medium (DMEM; Invitrogen, Carlsbad, CA), supplemented with 10% fetal bovine serum and Pen/Strep, and grown in an incubator with 5% CO_2 at 37°C. Four HCC tumor samples were harvested at the time of surgery. After digestion with type IV collagenase (100 units/mL; Sigma) at 37°C for 15 minutes, the tissues were minced and the cell suspension was passed through a 100-μM nylon mesh and placed into DMEM medium. Cells were cultured in log-growth phase in DMEM medium (Invitrogen), supplemented with 10% fetal bovine serum (Sigma) and grown in an incubator with 5% CO_2 at 37°C.

Retroviral Transduction of the Degron Reporter Into Human HCC Cells. The degron sequence of ODC is known to be directly recognized by the proteasome, which leads to the immediate destruction of the involved protein. A retroviral expression vector pQCXIN-ZsGreen-cODC, containing green fluorescent ZsGreen-labeled degron ODC (Gdeg), was kindly provided by Dr. Frank Pajonk. The vector was transfected into platinum retroviral packaging cells and the retrovirus collected from the supernatant was used to infect HCC cells. Stable transfectants were selected with G418 (Invitrogen), and the accumulation of ZsGreen-degron ODC protein (Gdeg) was monitored by fluorescence microscopy and flow cytometry (FITC channel). Stable transfection was confirmed by exposing the cells to the proteasome inhibitor MG-132 (Calbiochem, San Diego, CA) for 12 hours. The established cell lines (HuH7, Hep3B, HLF, and SK-Hep1) as well as one cell culture line derived from each of the four HCC tissues were successfully engineered to stably express Gdeg. Fluorescence microscopy was performed using Axio-Observer (Carl Zeiss, Oberkochen, Germany), and images were acquired digitally using AxioVision (Carl Zeiss).

Flow Cytometry and Cell Sorting. For the flow cytometry experiments the cell number was evaluated using a FACSCanto II (BD Biosciences), and cell sorting was performed using a FACSAria II (BD Biosciences). HCC cells were washed with phosphate-buffered saline (PBS), then enzymatically dissociated using 0.05% trypsin-EDTA (Invitrogen). Trypsinized cells were suspended in fluorescence activated cell sorting (FACS) buffer and analyzed on a FACSCanto II using FACSDiva software (BD Biosciences). For intracellular ROS analysis, cells were loaded with 5 mM MitoSOX

Abbreviations: CSC, cancer stem cells; FDR, false discovery rate; GSEA, gene set enrichment analysis; HCC, hepatocellular carcinoma; NOD/SCID, nonobese diabetic / severe combined immunodeficient; ODC, ornithine decarboxylase; ROS, reactive oxygen species.

From the [1]Department of Hepato-Biliary-Pancreatic Surgery, Graduate School of Medicine, Tokyo Medical and Dental University, Tokyo, Japan; [2]Department of Computational Biology, Graduate School, Tokyo Medical and Dental University, Tokyo, Japan; [3]Oxygen Biology Unit, Frontier Research Laboratory, Medical Research Institute Tokyo Medical and Dental University, Tokyo, Japan; [4]Department of Molecular Virology, Tokyo Medical and Dental University, Tokyo, Japan.

Received June 30, 2012; accepted February 13, 2013.

Supported by Grant-in-Aid for Scientific Research on Innovative Areas, Scientific Research (A), Project of Development of Innovative Research on Cancer Therapeutics from Ministry of Education, Culture, Sports, Science & Technology of Japan, and Health & Labour Sciences Research Grant from Ministry of Health Labour & Welfare of Japan.

Address reprint requests to: Shinji Tanaka, M.D., Ph.D., FACS, Department of Hepato-Biliary-Pancreatic Surgery, Graduate School of Medicine, Tokyo Medical and Dental University, 1-5-45 Yushima, Bunkyo-ku, Tokyo 113-8519, Japan. E-mail: shinji.msrg@tmd.ac.jp; fax: +81-3-5803-0263.

View this article online at wileyonlinelibrary.com.

DOI 10.1002/hep.26345

Potential conflict of interest: Nothing to report.

Additional Supporting Information may be found in the online version of this article.

Red (Invitrogen) at 37°C for 30 minutes and were immediately analyzed using FACSCanto II. $Gdeg^{high}ROS^{low}$ cells represented 0.16%-2.5% of the established HCC cell lines (Supporting Table 1). The percentage of $Gdeg^{high}ROS^{low}$ cells remained the same immediately after isolation by FACS, but increased to approximately 40% after time in culture (Supporting Fig. 4). For surface maker analysis, cells were labeled with allophycocyanin-conjugated antihuman CD44, CD90, EpCAM (BioLegend), and CD133/1 (MACS Miltenyi Biotec) antibodies. Labeled cells were immediately analyzed using FACSCanto II.

Time-Lapse Analysis. After FACS, $Gdeg^{high}$ or $Gdeg^{low}$ HCC cells were plated separately at a density of 10^4 cells in 6-cm dishes and in log-growth phase in 1640 RPMI medium (Invitrogen), supplemented with 10% fetal bovine serum (Sigma) and Pen/Strep (Sigma) as antibiotics. After incubation in 5% CO_2 at 37°C overnight, cell attachment was confirmed. Image analysis was performed using AxioVision and AxioObserver.

Treatment With Hypoxia or $CoCl_2$. HCC cells were exposed to hypoxic conditions (1% O_2, 5% CO_2, and 94% N_2) in an anaerobic workstation (Hirasawa Works, Tokyo, Japan). Oxygen concentration inside the workstation was constantly monitored by the oxygen sensor (MC-8G-S, Iijima Electrics, Gamagori, Japan) and maintained at 1% during the experiment. Cells (2.5×10^5) were grown with RPMI medium plus 3.5 g/L D-glucose in 10-cm dishes. The proportion of fluorescent cells was measured using FACSCanto II every 2 days. Cells were passaged every 6 days in an anaerobic workstation.

To further assess the effect of hypoxia on HCC cells, cells were treated with 100 μM $CoCl_2$ (Sigma) and/or 10 nM echinomycin (Sigma) added to the medium. After 24 and 48 hours, the proportion of fluorescence cells was measured using FACSCanto II. Chemosensitivity to the anticancer drug fluorouracil (5-FU) was analyzed using $Gdeg^{high}$ HuH7 and unsorted HuH7 cells under these hypoxia-mimicking condition. 5-FU was suspended in the culture media, serially diluted across 96-well microtiter plates (100 μL), and incubated at 37°C with 5% CO_2 for 48 hours. The number of living cells was measured using the MTS assay (Celltiter-Glo Luminescent Cell Viability Assay, Promega, Madison, WI), according to the manufacturer's instructions. The absorbance was read at 490 nm using a multiwell plate reader (Model 550, Bio-Rad, Richmond, CA), with wells containing medium but no cells serving as blank controls. Experiments were independently evaluated in triplicate.

Spheroid Assay. The spheroid assay was performed as described.[16] After FACS, $Gdeg^{high}$ or unsorted cells were plated separately at a density of 1,000 cells in low attachment plates (96-well Ultra Low Cluster Plate; Costar, Corning, NY) and incubated in serum-free DMEM/F12 medium (Invitrogen). For observation by time-lapse microscopy, 6-cm dishes were coated with poly-HEMA (20 mg/mL; Sigma). Image analysis was performed using AxioVision and AxioObserver.

Tumor Xenotransplantation and Tumorigenicity. Female NOD.CB17-PRkdc^{Scid}/J mice aged 4-6 weeks were purchased from Charles River Japan (Kanagawa, Japan). Various numbers of sorted $Gdeg^{high}ROS^{low}$ and unsorted HCC cells, ranging from 1×10^2 to 1×10^5 cells, were each mixed with 100 μL of Matrigel (BD Biosciences) and injected subcutaneously into both flanks of mice under anesthesia. Tumor formation was monitored every 2 days. All *in vivo* procedures were approved by the Animal Care Committee of Tokyo Medical and Dental University (Permission No. 090235).

RNA Extraction and Gene Expression Analysis. Total RNA was extracted from cancer and adjacent noncancerous tissues using the RNeasy kit (Qiagen, Hilden, Germany), and the integrity of obtained RNA was assessed using the Agilent 2100 Bioanalyzer (Agilent Technologies, Palo Alto, CA). All samples had an RNA Integrity Number greater than 5.0. Contaminant DNA was removed by digestion with RNase-free DNase (Qiagen). Complementary RNA was prepared from 2 μg of total RNA using 1-cycle target labeling and a control reagent kit (Affymetrix, Santa Clara, CA). Hybridization and signal detection of HG-U133 Plus 2.0 arrays (Affymetrix) were performed according to the manufacturer's instructions. The microarray datasets of (1) $Gdeg^{high}ROS^{low}$ and $Gdeg^{low}ROS^{high}$ HuH7 cells and (2) 253 tissue samples from HCC patients were normalized separately using the robust multiarray average method found in the R statistical software (v. 2.12.1) together with the Bioconductor package. Estimated gene-expression levels were obtained in log2-transformed values, and 62 control probe sets were removed for further analysis.

Gene Set Enrichment Analysis (GSEA). Biological functions associated with the malignant phenotype in HCC cells were investigated using GSEA v. 2.0.7 with MSigDB gene sets v. 3.0.[17] Probe sets marked as "present" by the Gene Expression Console software (Affymetrix) in at least one $Gdeg^{high}ROS^{low}$ or $Gdeg^{low}ROS^{high}$HuH7 cell were used for this analysis. Gene set category "C2 CP REACTOME," which is based on the Reactome database (http://www.reactome.org), was used. For analysis of the gene expression profiles obtained from HCC patients, a custom gene set was employed using genes showing more than a 2-fold change between $Gdeg^{high}ROS^{low}$ and $Gdeg^{low}ROS^{high}$ HuH7 cells. Gene sets satisfying both criteria with $P < 0.05$ and a false discovery rate (FDR) <0.05 were considered significant.

Macrophage Migration Assay. To determine whether tumor cells induce macrophage/monocyte chemotaxis, the double chamber migration assay was performed using the RAW264 murine macrophage cell line (RIKEN Cell Resource Center, Tsukuba, Japan). Briefly, the migration of RAW264 cells was assayed using a transwell chamber (24-well plate, 8-μm pore; BD Biosciences, Bedford, MA). In the lower chamber, 7.5×10^4 tumor cells in 0.8 mL of media were seeded and incubated in serum-free media for 72 hours. RAW264 cells (5×10^4 in 0.3 mL serum free media) were then seeded into the upper chamber and incubated at 37°C for 4 hours. RAW264 cells found on the upper surface of the filter were removed using a cotton wool swab. Cells were then fixed with 100% methanol and stained using Giemsa solution and the number of cells migrating to the lower surface was counted. Each experiment was conducted in triplicate and the mean is shown.

Peritoneal Metastasis Model. Peritoneal metastatic potentials of cancer cells were assessed as reported.[18] Briefly, 10^5 $Gdeg^{high}ROS^{low}$ HCC cells or unsorted control cells were injected intraperitoneally into 5-week-old female NOD.CB17-PRkdc^{Scid}/J mice (n = 4 mice per group; Charles River Japan, Kanagawa, Japan). The care and use of animals was in accordance with institutional guidelines. The mice were monitored three times weekly for lethargy, weight loss, and abdominal enlargement. Mice were euthanized by cervical dislocation at 4 weeks and the number and weight of tumor nodules within the peritoneal cavity were counted.

Immunofluorescent Staining. Tissue sections were prepared according to standard procedures. After deparaffinization, slides were incubated in permeabilization buffer (0.2% Triton-PBS) for 30 minutes, followed by incubation in blocking buffer (3% bovine serum albumin [BSA]-PBS) for 1 hour and exposure to the primary antibodies (F4/80 1:200, BioLegend) overnight at 4°C. Sections were then treated for 30 minutes with the secondary antibody Alexa Fluor 568 tetramethylrhodamine isothiocyanate-conjugated anti-rat IgG (1:1,000, Sigma) and Hoechst 33342 solution for nuclear staining diluted in PBS and 3% BSA. After mounting the slides were visualized with a fluorescent microscope (Carl Zeiss, Germany).

Protein Network Analysis. To reveal functional relationships among genes differentially expressed in $Gdeg^{high}ROS^{low}$ HuH7 cells, the protein interaction network was analyzed. Genes up-regulated or down-regulated more than 1.1-fold between $Gdeg^{high}ROS^{low}$ and $Gdeg^{low}ROS^{high}$HuH7 cells were included in the network. Protein interaction data obtained from BIND (http://bond.unleashedinformatics.com), BioGRID (http://thebiogrid.org), and HPRD (http://www.hprd.org) were downloaded from the ftp site of the National Center for Biotechnology Information (NCBI; ftp://ftp.ncbi.nih.gov/gene/GeneRIF/interactions.gz). The protein interaction network was analyzed using Cytoscape software.[19]

Patients and Tissue Samples. In all, 187 patients underwent curative hepatectomy for HCC from 2004 to 2007 at Tokyo Medical and Dental University Hospital (Tokyo, Japan), and among these, 153 cases were randomly selected for this study. With Institutional Review Board approval, written informed consent was obtained from all patients (Permission No. 1080). Noncancerous liver tissue adjacent to HCC (n = 100) was snap-frozen in liquid nitrogen and stored at −80°C. Patients were followed up with assays for serum alpha-fetoprotein levels and protein induced by vitamin K absence or antagonists-II every month and with ultrasonography, computed tomography, and magnetic resonance imaging every 3 months. Median observation time was 9.86 months.

To divide patients into subgroups based on expression profiles of a particular gene set, gene-set enrichment patterns were analyzed using a method similar to that described by Ben-Porath et al.[20] For each patient, the number of genes that showed more than a 1.1-fold change in expression (either up-regulation or down-regulation) compared to the mean expression levels were counted. Patients who exhibited up-regulation of more than 30% of the genes in the gene set were classified as the high expression group. Likewise, patients who showed down-regulation of more than 30% of the genes in the gene set were classified as the low expression group. Samples that satisfied neither or both criteria above were classified as the moderate expression group. The recurrence-free survival rates among three groups were compared by Kaplan-Meier curves, followed by the log-rank test.

Statistical Analysis. Experimental data are expressed as mean values with 95% confidence intervals (CI) and were compared using a two-sided paired Student's *t* test. Statistical significance was defined as $P < 0.05$.

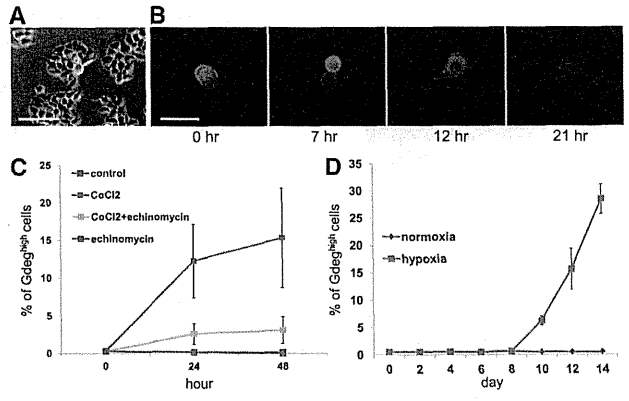

Fig. 1. (A) Frequency of cells with accumulation of Gdeg protein ($Gdeg^{high}$) in human HCC cultures (bar, 100 μm). (B) Asymmetric cell division of the $Gdeg^{high}$ HCC observed by time-lapse microscope. $Gdeg^{high}$ HCC cells asymmetrically divided into $Gdeg^{high}$ and $Gdeg^{low}$ HCC cells (bar, 50 μm). (C) The alteration of the $Gdeg^{high}$ proportion in the unsorted HCC cells after 24-hour and 48-hour treatment of $CoCl_2$ (100 μM) with or without echinomycin (10 nM); results are presented as means ± standard deviation from triplicate experiments. (D) The alteration of the $Gdeg^{high}$ proportion in the unsorted HCC cells under long-term hypoxic conditions (1% O_2); results are presented as means ± standard deviation from triplicate experiments.

Results

Characterization of CSC Proteasome Activity in Human HCC Cells. Human HCC cells were engineered to stably express ZsGreen-labeled degron (Gdeg) according to the previous report by Vlashi et al.[12] Cells displaying high levels of Gdeg ($Gdeg^{high}$) represented 0.5%-7.5% of the population in human HCC cell lines (Fig. 1A). In contrast, $Gdeg^{high}$ cells represented 0.1% of the population in human primary HCC (Supporting Fig. 1); however, only four generations were passaged without establishment. Isolation of the established $Gdeg^{high}$ cells and $Gdeg^{low}$ cells was performed using FACSAria II (BD Biosciences). As demonstrated by time-lapse microscopy, $Gdeg^{high}$ cells can asymmetrically divide into $Gdeg^{low}$ and $Gdeg^{high}$ cells, while $Gdeg^{low}$ cells never divide into $Gdeg^{high}$ cells. These results demonstrate some properties of CSCs and non-CSCs,[21] such as hierarchical division of CSCs and loss of stemness in differentiated non-CSCs (Fig. 1B; Supporting Video 1). In addition, the spheroid assay revealed that $Gdeg^{high}$ cells form slightly larger spheroids than unsorted cells (Supporting Fig. 2).

Effects of Hypoxia on HCC CSCs. Since pluripotent potentials in embryonic stem cells can be efficiently maintained under low oxygen levels[22] and hypoxia can contribute to CSC maintenance,[23] the effects of hypoxic conditions in unsorted HCC cells transfected with Gdeg were analyzed. The proportion of $Gdeg^{high}$ HCC cells significantly increased after 48-hour treatment with $CoCl_2$, an agent mimicking the activation of hypoxia-inducing factor (HIF).[24] The effects of $CoCl_2$ were blocked by echinomycin, a molecule inhibiting HIF-1 DNA binding activity (Fig. 1C) that has recently been reported to eradicate serially transplantable human acute myeloid leukemia (AML) in xenogeneic models by preferential elimination of CSCs.[25] The effects of long-term hypoxic treatment (1% O_2) were also analyzed in the unsorted HCC cells. $Gdeg^{high}$ cells represented 0.5% of the population on Day 1, but significantly increased to 28.0% on Day 14 (Fig. 1D). Similar to previous reports showing that CSCs are usually resistant to the conventional chemotherapy,[9] $Gdeg^{high}$ cells also demonstrated chemoresistance compared to unsorted cells under hypoxia conditions (Supporting Fig. 3). These results are consistent with reports showing that hypoxic conditions serve as a stimulus to reprogram cells towards normal stem cells and CSCs.[22,23]

CSCs Property of the HCC Subpopulation With Low Intracellular ROS Levels and Low Proteasome Activity. $Gdeg^{high}$ cells had a lower concentration of ROS than the unsorted cells based on the intracellular concentrations of MitoSOX Red staining. Intracellular ROS-positive cells (ROS^{high}) accounted for 71.0% ± 8.22% of the unsorted HuH7 HCC cells, but only 37.2% ± 10.8% within the $Gdeg^{high}$ HuH7 cell population ($P < 0.05$). The $Gdeg^{high}$ group also contained a subpopulation of cells with low intracellular ROS levels ($Gdeg^{high}ROS^{low}$) (Fig. 2A).

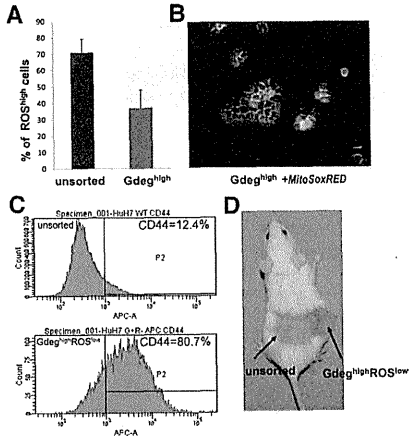

Fig. 2. (A) The proportion of ROS-positive cells (ROS^{high}) in unsorted HCC cells (left) and the sorted $Gdeg^{high}$ HCC cells (right) determined by FACS analysis with MitoSOX Red staining; results are presented as means ± standard deviation from triplicate experiments ($P < 0.05$). (B) $Gdeg^{high}$ and $Gdeg^{high}$ HCC cells stained with MitoSOX Red; (C) Flow cytometry histogram showing expression of CD44 positive cells in the $Gdeg^{high}ROS^{low}$ HuH7 cells (80.7%) and unsorted HuH7 cells (12.4%). (D) Tumorigenicity analysis using NOD/SCID mice; a tumor nodule was detected at the inoculation site of 10^2 $Gdeg^{high}ROS^{low}$ HCC cells, but not at the inoculation site of the unsorted cells.

To determine whether $Gdeg^{high}ROS^{low}$ HCC cells might possess certain stem cell-like properties, the expression of stem cell surface markers, CD133,[5] CD90,[6] EpCAM,[7] and CD44 was analyzed.[8] CD44-postiveness was detected in 80.7% of $Gdeg^{high}ROS^{low}$ HuH7 cells, but in only 12.4% of unsorted HuH7 cells (Fig. 2C). EpCAM and CD90 expression were increased in the $Gdeg^{high}ROS^{low}$ HLF cells compared to the unsorted HLF cells (EpCAM; 6.0% versus 2.7%, CD90; 55.9% versus 44.6%).

An important test for validating whether cells are CSCs is the identification of a cancer initiation population demonstrated by increased tumorigenicity *in vivo*. Different cell numbers from each population were injected subcutaneously into nonobese diabetic / severe combined immunodeficient (NOD/SCID) mice in numbers ranging from 10^2 to 10^5 cells per injection. $Gdeg^{high}ROS^{low}$ HCC cells had higher tumorigenic capacity than unsorted cells. As few as 10^2 $Gdeg^{high}ROS^{low}$ HCC cells could form a subcutaneous tumor (Fig. 2D, Table 1; Supporting Table 2). Cancer initiation frequency was calculated using L-Calc Software[26] (Stem Cell Technologies), and significance was determined by chi-square analysis using ELDA (Walter and Eliza Hall Bioinformatics).[26] The cancer initiation frequency was 1 in 2,083 (95% CI = 739 to 5,867) for $Gdeg^{high}ROS^{low}$ HCC cells and 1 in 79,189 (95% CI = 31,651 to 198,128) for unsorted cells ($P < 0.001$). These data validate that CSCs are significantly enriched in the $Gdeg^{high}ROS^{low}$ subpopulation compared to unsorted HCC cells.

Tumor-Host Interactions of HCC CSCs. Comprehensive gene expression analysis in $Gdeg^{high}ROS^{low}$ HCC cells was performed to acquire the CSC gene profile. As described in a previous report,[13] GSEA based on the Reactome database[27] was utilized to determine the biological pathways activated or inactivated in $Gdeg^{high}ROS^{low}$ HCC cells. The GSEA demonstrated significant enrichment in 8 gene sets (Supporting Table 3), and the gene set "chemokine_receptors_bind_chemokines" showed the lowest FDR (Fig. 3A). A protein interaction network was then constructed using 12,890 probe sets with at least 10% change in expression levels. To more closely investigate molecular networks associated with chemokines, a subnetwork of 2-hop neighbors from chemokine ligands and receptors including CXCL, CCL, CX3CL, XCL, CXCR, CCR, CX3CR, and XCR family genes was generated (Fig. 3B).

The ability of $Gdeg^{high}ROS^{low}$ HCC cells to induce macrophage chemotaxis was determined using a chemotaxis assay and the RAW264 murine macrophage-like cell line (Fig. 3C). $Gdeg^{high}ROS^{low}$ HCC cells significantly facilitated RAW264 cell migration compared to their counterparts and unsorted controls (average number of cells that migrated to the lower chamber, $Gdeg^{high}ROS^{low}$ HCC cells versus unsorted HCC cells: difference = 192, 95% CI = 61 to 323, $P = 0.0153$, n = 3; $Gdeg^{high}ROS^{low}$ HCC cells versus $Gdeg^{low}ROS^{high}$ HCC cells: difference = 196, 95%

Table 1. Enhanced Tumor Formation by $Gdeg^{high}ROS^{low}$ HCC Cells

Number of Cells Injected	Fraction (%) of Injected Mice That Developed Tumors: Injected With $Gdeg^{high}ROS^{low}$ Cells	Injected With Unsorted Cells
10^2	3/6 (50%)	0/6 (0%)
10^3	4/6 (66.7%)	1/6 (16.7%)
10^4	5/6 (83.3%)	2/6 (33.3%)
10^5	5/6 (83.3%)	3/6 (50%)

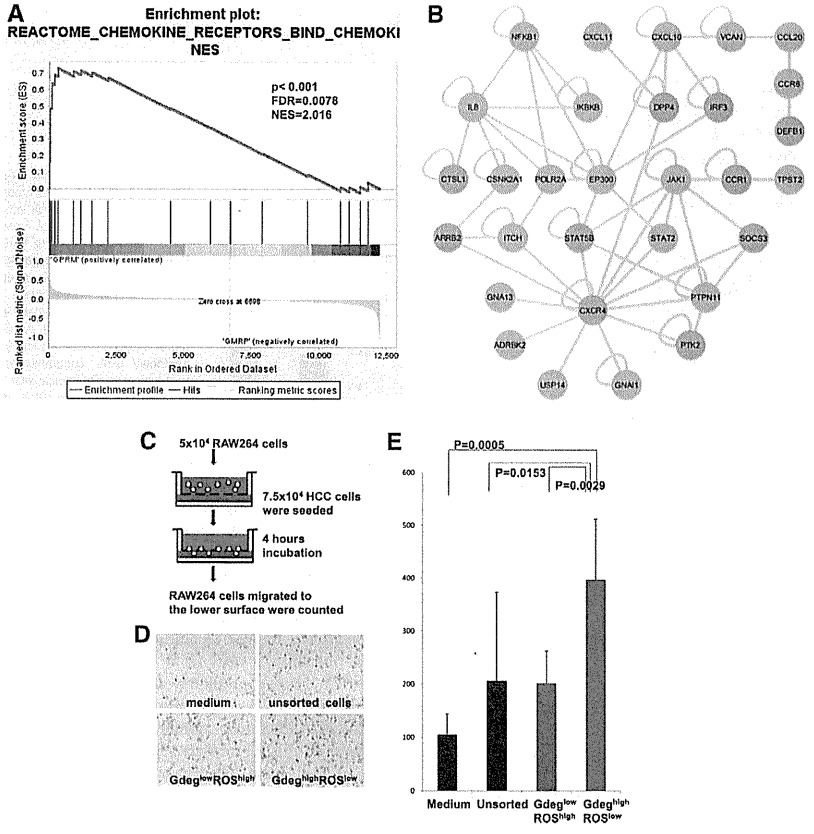

Fig. 3. (A) GSEA evaluation of gene-expression profile associated with Gdeg^{high}ROS^{low} HCC cells; the gene set "chemokine_receptors_bind_-chemokines" showed the lowest FDR ($P < 0.001$; FDR = 0.0078; NES = 2.016). (B) A protein interaction network constructed using 12,890 probe sets with at least 10% change in expression levels; a sub-network of 2-hop neighbors from chemokine ligands and receptors was extracted. (C) Diagram of the double chamber migration assay using a RAW264 murine macrophage-like cell line. (D) Giemsa staining for the RAW264 cells migrating to the lower surface. (E)The number of the RAW264 cells migrated to the lower surface induced by Gdeg^{high}ROS^{low} HCC cells compared to Gdeg^{low}ROS^{high} HCC cells, unsorted HCC cells, and medium. Each experiment was conducted in triplicate, and data are presented as the means ± 95% CI.

CI = 112 to 280, $P = 0.0029$, n = 3, Gdeg^{high}ROS^{low} HCC cells versus medium: difference = 292, 95% CI = 214 to 370, $P < 0.001$, n = 3) (Fig. 3D,E). Facilitated migration of host macrophages may be associated with niche formation of the HCC CSCs subpopulation.

To investigate whether the HCC cells established *in vivo* metastasis, Gdeg^{high}ROS^{low} or unsorted HCC cells were administered intraperitoneally in a NOD/SCID mouse model, as described previously.[18] Peritoneal metastases were assessed by counting the number of nodules and evaluating tumor weight in the mesentery and peritoneal walls. The tumor weight (average weight of dissemination nodules: Gdeg^{high}ROS^{low} HCC cells versus unsorted HCC cells, difference = 0.197, 95% CI = −0.304 to 0.699, $P = 0.3728$,

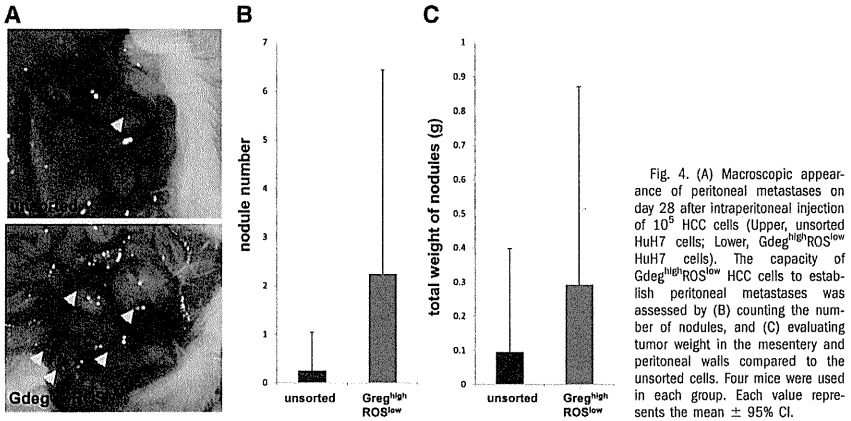

Fig. 4. (A) Macroscopic appearance of peritoneal metastases on day 28 after intraperitoneal injection of 10^5 HCC cells (Upper, unsorted HuH7 cells; Lower, Gdeg^{high}ROS^{low} HuH7 cells). The capacity of Gdeg^{high}ROS^{low} HCC cells to establish peritoneal metastases was assessed by (B) counting the number of nodules, and (C) evaluating tumor weight in the mesentery and peritoneal walls compared to the unsorted cells. Four mice were used in each group. Each value represents the mean ± 95% CI.

n = 4; Fig. 4B) and number (average number of dissemination nodules: Gdeg^{high}ROS^{low} HCC cells versus unsorted HCC cells, difference = 2.00, 95% CI = −1.28 to 5.28, $P = 0.1857$, n = 4; Fig. 4C) of the Gdeg^{high}ROS^{low} HCC cells group were higher than those in the unsorted group. Immunofluorescent analysis revealed that murine macrophages had infiltrated around the Gdeg^{high} HCC cells located at the metastatic tumor margins, indicative of the ability of these cells to recruit macrophages *in vivo* (Fig. 5).

Clinical Implication of the Gene Signature Up-Regulated in HCC CSCs. The clinical implication of the HCC CSC gene signature was retrospectively assessed using liver tissues from patients who received curative resection of HCC. CSC-gene signatures were generated as 43 probe sets using the gene expression profiles up-regulated in Gdeg^{high}ROS^{low} HCC cells (Supporting Table 4) and revealed a significant correlation between the noncancerous liver gene expressions and the CSC-gene signatures ($P = 0.004$ and FDR = 0.005; Fig. 6A). CSC-gene signatures were then evaluated with regard to patient outcomes. Patients were divided into three subtypes; high, moderate, and low expression groups, on the basis of expression profiles of the 43 CSC-related probe sets (Fig. 6B). These three groups showed significant differences in recurrence-free survival rates ($P = 0.002$ by log-rank test; Fig. 6C). High expression was significantly associated with diminished liver function (low albumin and high bilirubin) and tumor number (Supporting Fig. 5). Expression of CSC markers (CD133, EpCAM, CD44, and CD90)[5-8] and biliary/progenitor cell markers (cytokeratin 7 and cytokeratin 19)[28] was also up-regulated in the high expression group (Supporting Fig. 6).

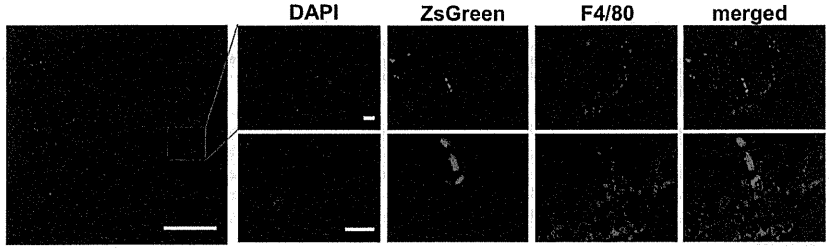

Fig. 5. Immunofluorescence of metastatic tumor sections labeled with antimouse F4/80 (bars, 1,000 μm (white) and 100 μm (yellow)); murine macrophages infiltrated around the Gdeg^{high} HuH7 cells located at the margins of the metastatic tumors.

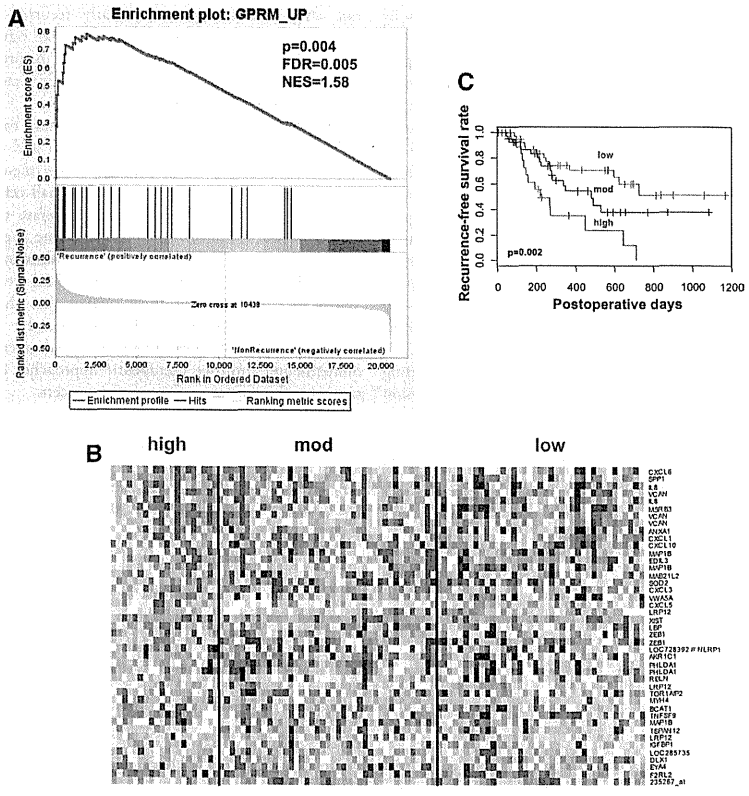

Fig. 6. (A) GSEA evaluation of the adjacent nontumor tissues; a positive correlation was observed between the gene set of Gdeg^{high}ROS^{low} HCC gene signature and noncancerous liver gene expression ($P < 0.004$; FDR = 0.005; NES = 1.58). (B) Patients were divided into three subtypes based on the expression profiles of 43 up-regulated probe sets of Gdeg^{high}ROS^{low} HCC. (C) A significant correlation was observed between the Gdeg^{high}ROS^{low} HCC gene signature and the recurrence-free survival rates of the patients after curative resection of HCC ($P = 0.002$).

Recently, leukemia CSC-specific gene signatures were revealed as highly independent predictors of patient survival.[29] This gene signature analysis demonstrates the clinical significance of identifying CSC populations in HCC using the stem-cell monitoring system described here.

Discussion

The monitoring system of stemness proposed here visualized two stem cell features, low proteasome activity and low ROS levels, in human HCC. Monitoring HCC proteasome activity revealed that human HCC cells contain a small population of cells that undergo asymmetric division, exhibiting the multipotency and self-renewal of CSCs (Fig. 1B).[20] Next, we showed that $CoCl_2$, an agent mimicking the activation of HIF,[24] increased the proportion of Gdeg^{high} HCC cells, indicative of low proteasome activity, while echinomycin, a molecule that inhibits HIF-1 DNA binding activity, blocked this effect (Fig. 1C). Recently, echinomycin was also reported to eradicate serially

transplantable human AML in xenogeneic models by preferential elimination of CSCs.[25] Similar to $CoCl_2$ treatment, hypoxic conditions also increased the proportion of Gdeg^{high} HCC cells (Fig. 1D), consistent with a previous report indicating that hypoxia serves as a stimulus to reprogram cells towards normal stem cells[22] and CSCs.[23] Additionally, HCC cells had an ROS concentration lower than that of unsorted HCC cells, including a subpopulation of Gdeg^{high} HCC cells (Gdeg^{high}ROS^{low}), in agreement with a previous report showing that normal stem cells and CSCs contain a lower concentration of ROS than their more mature progeny.[14] Importantly, xenotransplantation experiments revealed that cells with increased tumorigenicity were significantly concentrated in the subpopulation of Gdeg^{high}ROS^{low} HCC cells.

An HCC stem cell-specific signature (Supporting Table 4) was identified by genome-wide expression analysis, and GSEA based on the Reactome data base[27] showed that our HCC stem cell system significantly correlated with the chemokine network (Fig. 3A,B; Supporting Table 3). Inflammatory mediators and cells are indispensable components of tumor-host interactions,[30] and studies have shown that cancer cell-secreted factors generate an inflammatory niche hospitable for progression and metastasis of cancer.[31,32] More recent studies have shown that glioma-initiating cells produced inflammatory mediators such as chemokines that induce tumor-associated macrophages to organize the glioma-initiating cells niche.[33] Macrophages are an important component of the tumor-host interaction that controls the survival, migration, and growth of metastatic cells.[34] Our data showed that Gdeg^{high}ROS^{low} HCC cells induced macrophage chemotaxis more effectively than their counterparts (Fig. 3E). Furthermore, these cells had a higher capacity for dissemination in an *in vivo* peritoneal metastasis model (Fig. 4B,C). We also found macrophage infiltration around the CSCs located at the margin of the dissemination tumor (Fig. 5), indicative of the ability of HCC CSCs to recruit macrophages *in vivo*.

Recent studies on murine breast CSCs have revealed that the tumor-host interaction plays a critical role in metastatic colonization of cancer cells.[35] It is noteworthy that the tumor-host interaction mediated by HCC CSCs is potentially associated with metastatic initiation in our study. The host gene expression signature of the noncancerous microenvironment is closely associated with prediction of HCC recurrence[36] and lung adenocarcinoma.[37] As a result, the gene expression signature of our HCC stem cells (Supporting Table 4) significantly correlates with the disease-free survival rate after radical surgery and early recurrence (Fig. 6A). These findings strongly suggest that our HCC stem cell monitoring system is useful in predicting clinical prognosis, and the validity of this system was further confirmed (Fig. 6C).

Our HCC CSCs system, which monitors two stem cell features, is a promising tool to extract and identify CSCs in live bodies and histological specimens. This system demonstrated the presence of a small cell population with an increased capacity to generate dissemination *in vivo*. Clinically, the gene signature specifically expressed in our HCC stem cells significantly correlated with HCC recurrence after radical resection. Taken together, these findings suggest that this stem cell monitoring system could illuminate the *in vivo* significance of CSC-host interactions and microenvironments and improve therapeutic approaches for metastasis and recurrence of aggressive cancers.

Acknowledgment: The authors thank Drs. Frank Pajonk and Erina Vlashi at the University of California for providing the pQCXIN-ZsGreen-cODC plasmid, Dr. Hideshi Ishii at Osaka University for providing the primary HCC cell cultures, and Ms. Ayumi Shioya for technical assistance.

References

1. Zhu AX, Duda DG, Sahani DV, Jain RK. HCC and angiogenesis: possible targets and future directions. Nat Rev Clin Oncol 2011;8:292-301.
2. Arii S, Yamaoka Y, Futagawa S, Inoue K, Kobayashi K, Kojiro M, et al. Results of surgical and nonsurgical treatment for small-sized hepatocellular carcinomas: a retrospective and nationwide survey in Japan. The Liver Cancer Study Group of Japan. HEPATOLOGY 2000;32:1224-1229.
3. Shrager B, Jibara G, Schwartz M, Roayaie S. Resection of hepatocellular carcinoma without cirrhosis. Ann Surg 2012;255:1135-1143.
4. Reya T, Morrison SJ, Clarke MF, Weissman IL. Stem cells, cancer, and cancer stem cells. Nature 2001;414:105-111.
5. Ma S, Chan KW, Hu L, Lee TK, Wo JY, Ng IO, et al. Identification and characterization of tumorigenic liver cancer stem/progenitor cells. Gastroenterology 2007;132:2542-2556.
6. Yang ZF, Ho DW, Ng MN, Lau CK, Yu WC, Ngai P, et al. Significance of CD90+ cancer stem cells in human liver cancer. Cancer Cell 2008;13:153-166.
7. Yamashita T, Ji J, Budhu A, Forgues M, Yang W, Wang HY, et al. EpCAM-positive hepatocellular carcinoma cells are tumor-initiating cells with stem/progenitor cell features. Gastroenterology 2009;136:1012-1024.
8. Zhu Z, Hao X, Yan M, Yao M, Ge C, Gu J, et al. Cancer stem/progenitor cells are highly enriched in CD133+CD44+ population in hepatocellular carcinoma. Int J Cancer 2010;126:2067-2078.
9. Clevers, H. The cancer stem cell: premises, promises and challenges. Nat Med 2011;17:313-319.
10. Murata S, Yashiroda H, Tanaka K. Molecular mechanisms of proteasome assembly. Nat Rev Mol Cell Biol 2009;10:104-115.
11. Hernebring M, Brolén G, Aguilaniu H, Semb H, Nyström T. Elimination of damaged proteins during differentiation of embryonic stem cells. Proc Natl Acad Sci U S A 2006;103:7700-7705.

12. Vlashi E, Kim K, Lagadec C, Donna LD, McDonald JT, Eghbali M, et al. In vivo imaging, tracking, and targeting of cancer stem cells. J Natl Cancer Inst 2009;101:350-359.
13. Tanaka S, Mogushi K, Yasen M, Ban D, Noguchi N, Irie T, et al. Oxidative stress pathways in noncancerous human liver tissue to predict hepatocellular carcinoma recurrence: a prospective, multicenter study. HEPATOLOGY 2011;54:1273-1281.
14. Merchant AA, Singh A, Matsui W, Biswal S. The redox-sensitive transcription factor Nrf2 regulates murine hematopoietic stem cell survival independently of ROS levels. Blood 2011;118:6572-6579.
15. Diehn M, Cho RW, Lobo NA, Kalisky T, Dorie MJ, Kulp AN, et al. Association of reactive oxygen species levels and radioresistance in cancer stem cells. Nature 2009;458:780-783.
16. Adikrisna R, Tanaka S, Muramatsu S, Aihara A, Ban D, Ochiai T, et al. Identification of pancreatic cancer stem cells and selective toxicity of chemotherapeutic agents. Gastroenterology 2012;143:234-45.
17. Subramanian A, Tamayo P, Mootha VK, Mukherjee S, Ebert BL, Gillette MA, et al. Gene set enrichment analysis: a knowledge-based approach for interpreting genome-wide expression profiles. Proc Natl Acad Sci U S A 2005;102:15545-15550
18. Tanaka S, Pero SC, Taguchi K, Shimada M, Mori M, Krag DN, et al. Specific peptide ligand for Grb7 signal transduction protein and pancreatic cancer metastasis. J Natl Cancer Inst 2006;98:491-498.
19. Smoot ME, Ono K, Ruscheinski J, Wang PL, Ideker T. Cytoscape 2.8: new features for data integration and network visualization. Bioinformatics 2011;27:431-432.
20. Ben-Porath I, Thomson MW, Carey VJ, Ge R, Bell GW, Regev A, et al. An embryonic stem cell-like gene expression signature in poorly differentiated aggressive human tumors. Nat Genet 2008;40:499-507.
21. Knoblich JA. Asymmetric cell division: recent developments and their implications for tumour biology. Nat Rev Mol Cell Biol 2010;11: 849-860.
22. Yoshida Y, Takahashi K, Okita K, Ichisaka T, Yamanaka S. Hypoxia enhances the generation of induced pluripotent stem cells. Cell Stem Cell 2009;5:237-241.
23. Li Z, Bao S, Wu Q, Wang H, Eyler C, Sathornsumetee S, et al. Hypoxia-inducible factors regulate tumorigenic capacity of glioma stem cells. Cancer Cell 2009;15:501-513.
24. Pacary E, Legros H, Valable S, Duchatelle P, Lecocq M, Petit E, et al. Synergistic effects of $CoCl_2$ and ROCK inhibition on mesenchymal stem cell differentiation into neuron-like cells. J Cell Sci 2006;119: 2667-2678.
25. Wang Y, Liu Y, Malek SN, Zheng P, Liu Y. Targeting HIF1α eliminates cancer stem cells in hematological malignancies. Cell Stem Cell 2011;8: 399-411.
26. Ishizawa K, Rasheed ZA, Karisch R, Wang Q, Kowalski J, Susky E, et al. Tumor-initiating cells are rare in many human tumors. Cell Stem Cell 2010;7:279-282.
27. Croft D, O'Kelly G, Wu G, Haw R, Gillespie M, Matthews L, et al. Reactome: a database of reactions, pathways and biological processes. Nucleic Acids Res 2011;39:D691-697.
28. Durnez A, Verslype C, Nevens F, Fevery J, Aerts R, Pirenne J, et al. The clinicopathological and prognostic relevance of cytokeratin 7 and 19 expression in hepatocellular carcinoma. A possible progenitor cell origin. Histopathology 2006;49:138-151.
29. Eppert K, Takenaka K, Lechman ER, Waldron L, Nilsson B, van Galen P, et al. Stem cell gene expression programs influence clinical outcome in human leukemia. Nat Med 2011;17:1086-1093.
30. Mantovani A, Allavena P, Sica A, Balkwill F. Cancer-related inflammation. Nature 2008;454:436-444.
31. Kim S, Takahashi H, Lin WW, Descargues P, Grivennikov S, Kim Y, et al. Carcinoma-produced factors activate myeloid cells through TLR2 to stimulate metastasis. Nature 2009;457:102-106.
32. Karnoub AE, Dash AB, Vo AP, Sullivan A, Brooks MW, Bell GW, et al. Mesenchymal stem cells within tumour stroma promote breast cancer metastasis. Nature 2007;449:557-563.
33. Yi L, Xiao H, Xu M, Ye X, Hu J, Li F, et al. Glioma-initiating cells: a predominant role in microglia/macrophages tropism to glioma. J Neuroimmunol 2011;232:75-82.
34. Qian B, Deng Y, Im JH, Muschel RJ, Zou Y, Li J, et al. A distinct macrophage population mediates metastatic breast cancer cell extravasation, establishment and growth. PLoS One 2009;4:e6562.
35. Malanchi I, Santamaria-Martínez A, Susanto E, Peng H, Lehr HA, Delaloye JF, et al. Interactions between cancer stem cells and their niche govern metastatic colonization. Nature 2011;481:85-89.
36. Budhu A, Forgues M, Ye QH, Jia HL, He P, Zanetti KA, et al. Prediction of venous metastases, recurrence, and prognosis in hepatocellular carcinoma based on a unique immune response signature of the liver microenvironment. Cancer Cell 2006;10:99-111.
37. Seike M, Yanaihara N, Bowman ED, Zanetti KA, Budhu A, Kumamoto K, et al. Use of a cytokine gene expression signature in lung adenocarcinoma and the surrounding tissue as a prognostic classifier. J Natl Cancer Inst 2007 15;99:1257-1269.

OPEN ACCESS Freely available online

PLOS | ONE

Cytoplasmic Location of α1A Voltage-Gated Calcium Channel C-Terminal Fragment ($Ca_v2.1$-CTF) Aggregate Is Sufficient to Cause Cell Death

Makoto Takahashi[1], Masato Obayashi[1], Taro Ishiguro[1], Nozomu Sato[1], Yusuke Niimi[1], Kokoro Ozaki[1], Kaoru Mogushi[2], Yasen Mahmut[2], Hiroshi Tanaka[2], Fuminori Tsuruta[3¤], Ricardo Dolmetsch[3], Mitsunori Yamada[5,6], Hitoshi Takahashi[5], Takeo Kato[7], Osamu Mori[8], Yoshinobu Eishi[4], Hidehiro Mizusawa[1], Kinya Ishikawa[1]*

1 Department of Neurology and Neurological Science, Graduate School, Tokyo Medical and Dental University, Yushima, Bunkyo-ku, Tokyo, Japan, 2 Information Center for Medical Sciences, Tokyo Medical and Dental University, Yushima, Bunkyo-ku, Tokyo, Japan, 3 Department of Neurobiology, Stanford University School of Medicine, Fairchild Research Building, Palo Alto, California, United States of America, 4 Department of Pathology, Graduate School, Tokyo Medical and Dental University, Yushima, Bunkyo-ku, Tokyo, Japan, 5 Department of Pathology, Pathological Neuroscience Branch, Brain Research Institute, Niigata University, Asahi-machi-dori, Niigata, Japan, 6 Department of Clinical Research, National Hospital Organization, Saigata National Hospital, Saigata, Ohgata-ku, Johetsu-City, Niigata, Japan, 7 Department of Neurology, Hematology, Metabolism, Endocrinology and Diabetology, Yamagata University Faculty of Medicine, Iida-Nishi, Yamagata, Japan, 8 Department of Internal Medicine and Neurology, Hatsuishi Hospital, Nishihara, Kashiwa, Chiba, Japan

Abstract

The human α_{1A} voltage-dependent calcium channel ($Ca_v2.1$) is a pore-forming essential subunit embedded in the plasma membrane. Its cytoplasmic carboxyl(C)-tail contains a small poly-glutamine (Q) tract, whose length is normally 4~19 Q, but when expanded up to 20~33Q, the tract causes an autosomal-dominant neurodegenerative disorder, spinocerebellar ataxia type 6 (SCA6). A recent study has shown that a 75-kDa C-terminal fragment (CTF) containing the polyQ tract remains soluble in normal brains, but becomes insoluble mainly in the cytoplasm with additional localization to the nuclei of human SCA6 Purkinje cells. However, the mechanism by which the CTF aggregation leads to neurodegeneration is completely elusive, particularly whether the CTF exerts more toxicity in the nucleus or in the cytoplasm. We tagged recombinant (r)CTF with either nuclear-localization or nuclear-export signal, created doxycyclin-inducible rat pheochromocytoma (PC12) cell lines, and found that the CTF is more toxic in the cytoplasm than in the nucleus, the observations being more obvious with Q28 (disease range) than with Q13 (normal-length). Surprisingly, the CTF aggregates co-localized both with cAMP response element-binding protein (CREB) and phosphorylated-CREB (p-CREB) in the cytoplasm, and Western blot analysis showed that the quantity of CREB and p-CREB were both decreased in the nucleus when the rCTF formed aggregates in the cytoplasm. In human brains, polyQ aggregates also co-localized with CREB in the cytoplasm of SCA6 Purkinje cells, but not in other conditions. Collectively, the cytoplasmic $Ca_v2.1$-CTF aggregates are sufficient to cause cell death, and one of the pathogenic mechanisms may be abnormal CREB trafficking in the cytoplasm and reduced CREB and p-CREB levels in the nuclei.

Citation: Takahashi M, Obayashi M, Ishiguro T, Sato N, Niimi Y, et al. (2013) Cytoplasmic Location of α1A Voltage-Gated Calcium Channel C-Terminal Fragment ($Ca_v2.1$-CTF) Aggregate Is Sufficient to Cause Cell Death. PLoS ONE 8(3): e50121. doi:10.1371/journal.pone.0050121

Editor: J. David Spafford, University of Waterloo, Canada

Received December 16, 2011; **Accepted** October 17, 2012; **Published** March 7, 2013

Funding: This study was funded by the Japanese Ministry of Education, Sports and Culture (KI and HM), the Japan Society for Promotion of Science (JSPS) (KI and HM), the 21st Century COE Program on Brain Integration and Its Disorders from the Japanese Ministry of Education, Science and Culture (HM), the Strategic Research Program for Brain Sciences by the Ministry of Education, Culture, Sports, Science and Technology of Japan (HM) and from the Health and Labour Sciences Research Grants on Ataxic Diseases (HM) of the Japanese Ministry of Health, Labour and Welfare, Japan. The funders had no role in study design, data collection and analysis, decision to publish, or preparation of the manuscript.

Competing Interests: The authors have declared that no competing interests exist.

* E-mail: pico.nuro@tmd.ac.jp

¤ Current address: Graduate School of Life and Environmental Sciences, University of Tsukuba, Tennodai, Tsukuba, Ibaraki, Japan

Introduction

Polyglutamine (polyQ) disease is a group of nine neurodegenerative disorders that are associated with protein aggregation caused by an expansion of the polyQ tract. These disorders include Huntington's disease (HD), spinobulbar muscular atrophy (SBMA), dentatorubral-pallidoluysian atrophy (DRPLA) and spinocerebellar ataxia (SCA) types 1, 2, 3, 6, 7, and 17 (SCA3 is also known as Machado-Joseph disease (MJD)) [1,2]. In general, the length of the polyQ tract encoded by trinucleotide (CAG) repeat is below 35 in normal individuals. In these diseases, however, the CAG repeat is expanded above 35 to even more than 100, which gives rise to a mutated protein with an expanded polyQ tract that tends to adopt a β-sheet structure, become misfolded, and form oligomers of mutated protein eventually forming microscopic aggregates.

The polyQ expansion causing SCA6 exists in the cytoplasmic carboxyl(C)-tail of the α_{1A} (P/Q-type) voltage-dependent calcium channel protein ($Ca_v2.1$) [3]. The cardinal clinical feature of SCA6 is progressive cerebellar ataxia with an average age-of-onset at 45.5 years and gaze-evoked nystagmus [4,5]. The Purkinje cell of the cerebellar cortex, which expresses $Ca_v2.1$ most abundantly in the brain, undergoes degeneration [5,6]. Previous studies have shown that the polyQ expansion in $Ca_v2.1$ causes functional alterations of $Ca_v2.1$ [7–10]. However, such functional alterations are not considered critical for SCA6 pathogenesis, as $Ca_v2.1$ functions were not obviously altered in two independent studies on knock-in mice [11,12]. Probably more important for the pathogenesis of SCA6 is the formation of microscopic aggregation of $Ca_v2.1$, which has been demonstrated in SCA6 human Purkinje cells by using several antibodies against the $Ca_v2.1$ C-terminus [6,13]. SCA6 has several unique features that make it appear as a different disorder among the rest of other polyQ diseases. First, the length of the polyQ tract in the $Ca_v2.1$ that is responsible for SCA6 falls within the normal range of repeats for other polyQ diseases (4–19 CAG/polyQs in the $Ca_v2.1$ of normal individuals compared with 20–33 CAG/polyQs in SCA6 subjects) [14,15]. Secondly, microscopic $Ca_v2.1$ aggregates can be seen in the cytoplasm (i.e., the cell body or cell processes) of SCA6 Purkinje cells, whereas in other polyQ diseases, aggregates with expanded polyQ are prevalent in the nuclei rather than in the cytoplasm of neurons expressing the responsible proteins [16,17]. These could indicate that SCA6 has a distinct underlying pathophysiology among polyQ diseases. Recently, a study by Western blot analysis showed that a 75-kDa $Ca_v2.1$ C-terminal fragment (CTF), thought to be generated by a proteolytic cleavage of the full-length $Ca_v2.1$, might have a critical role in SCA6 pathogenesis from the following reasons [18]. First, the CTF with a normal-length polyQ tract remains soluble and is localized exclusively in the cytosolic fraction of the normal human cerebellum. Second, the CTF becomes insoluble in the cytosolic fraction of SCA6 cerebellum. Third, a small amount of CTF is additionally detected in the nuclear fraction in the human SCA6 cerebellum, suggesting that the expansion of polyQ causes the CTF to translocate into the nucleus as well as to aggregate in the cytoplasm. These findings raise a fundamental question: where (i.e., the nucleus or the cytoplasm) does the CTF exert serious toxicity? In this context, two previous studies reported that a recombinant (r)CTF, when expressed in cultured cells, tends to localize into the nuclei and exert toxicity in the nucleus rather than in the cytoplasm [19,20]. However, two other studies demonstrated completely opposite data that the rCTF predominantly locates in the cytoplasm where it exerts toxicity [18,21]. We therefore investigated the relationship between the location of CTF and cell death by using newly created cultured cell models. In addition, we also pursued alterations in protein expression and intracellular localization of the cAMP response element-binding protein (CREB) suggested by the pathogenesis of other polyQ diseases. We finally asked whether the findings in cultured cells are relevant to the human SCA6 pathology. Here we show that the CTF with expanded polyQ is sufficient to cause toxicity in the cytoplasm.

Results

Nuclear localization signal (NLS) and nuclear export signal (NES) faithfully targeted the CTF to the desired intracellular locations

We first asked the primary location of the rCTF. We avoided using the enhanced green-fluorescent protein (EGFP), since a large proportion of the rCTF-polyQ (either Q13 or Q28) dramatically shifted into the nucleus with the presence of EGFP (Figure S1A, S1B, S1C). Instead, we utilized an artificial nuclear localization signal (NLS) and export signal (NES), to regulate the location of the rCTFs (Figure 1A). Two types of polyQ (Q13: normal, Q28: expanded) were used (Figure 1A). We fused the rCTFs with either NLS or NES, transfected each of these in PC12 cells, and then examined the intracellular distributions of these constructs. The rCTF-Q13, the normal version of CTF with an approximate size of 75–80 kDa [18], was predominantly, though not exclusively, expressed in the cytoplasm. In the presence of the NLS tag, the rCTF-Q13-NLS dramatically translocated to the nucleus, whereas the NES tag made the rCTF-Q13-NES anchor in the cytoplasm (Figure 1B). This result was confirmed in human embryonic kidney (HEK) 293T cells (Figure S2), and was consistent with the location of native CTF in human brain [18]. The expanded version of the CTF, rCTF-Q28 was also expressed mainly in the cytoplasm with some obvious amounts in the nucleus (Figure 1C). In contrast, the rCTF-Q28 tagged with NLS showed much stronger tendency to locate in the nuclei, while the rCTF-Q28 tagged with NES appeared to remain entirely in the cytoplasm, showing that both NLS and NES are efficient signals to make the rCTF confine in a desired location. When the intracellular locations of various rCTFs were rated into 4 groups (N: exclusively seen in the nucleus; N-c: predominantly located in the nucleus; n-C: predominantly located in the cytoplasm; C: exclusively seen in the cytoplasm)(*See, Materials and Methods for details*), the effects of NLS and NES were confirmed (Figure 1D). This allowed us to examine the roles of CTF in the nucleus and in the cytoplasm separately by using the NLS and NES.

rCTF-NES/-NLS stably expressed in PC12 cell lines with doxycyclin removal

To clarify the chronological sequence of the CTF expression, the formation of CTF aggregates and the point of cell death, we created PC12 cell lines that stably expressed the rCTF by removing the doxycyclin (Dox) (Tet-off PC12 system). In basal conditions when the Dox is kept added in culture medium, Tet-off PC12 cells do *not* express rCTF (termed "Dox(+)" condition). However, when the culture medium was replaced with the one lacking the Dox, cells began to express rCTFs (termed "Dox(−)" condition). Taking an advantage of the fact that the PC12 cells differentiate into cells with neuronal characteristics on exposure to the nerve-growth factor (NGF), we added the NGF and removed the Dox at the same day, which we designate "Day0". We chose six stable PC12 cell clones (rCTF-Q13, rCTF-Q13-NLS, rCTF-Q13-NES, rCTF-Q28, rCTF-Q28-NLS, rCTF-Q28-NES), which had been confirmed to express equivalent rCTF levels by quantitative real-time reverse-transcription PCR (qRT-PCR) (*data shown upon request*). At the mRNA level, the quantitative RT-PCR showed that the rCTF mRNA level starts to be detected from Day3 (Figure 2A). At the protein level, Western analysis using the A6RPT-#5803 antibody against the C-terminus of $Ca_v2.1$ [18] showed that the rCTF expression starts to be detected on the fourth day after Dox removal ("Day4") and reaches abundant levels by Day6 (Figure 2B). The maximum protein expression level at Day6 was approximately 10% of that expressed in transiently over-expressed PC12 cells (*data shown upon request*).

The fluorescent immunocytochemistry revealed that in the stable PC12 cells expressing rCTF-Q28-NES, the recombinant protein was expressed mainly in the cytoplasm (Figure 2C, upper panels), whereas in stable PC12 cells expressing rCTF-Q28-NLS, the protein was confined to the nucleus (Figure 2C, lower panels). The restricted intracellular distribution by NES and NLS was also confirmed by Western blotting (Figure 2D).

We next searched the timeline of the formation of rCTF aggregates. In PC12 cells expressing rCTF-Q28-NES, the cytoplasmic rCTF aggregates visualized by using A6RPT-#5803

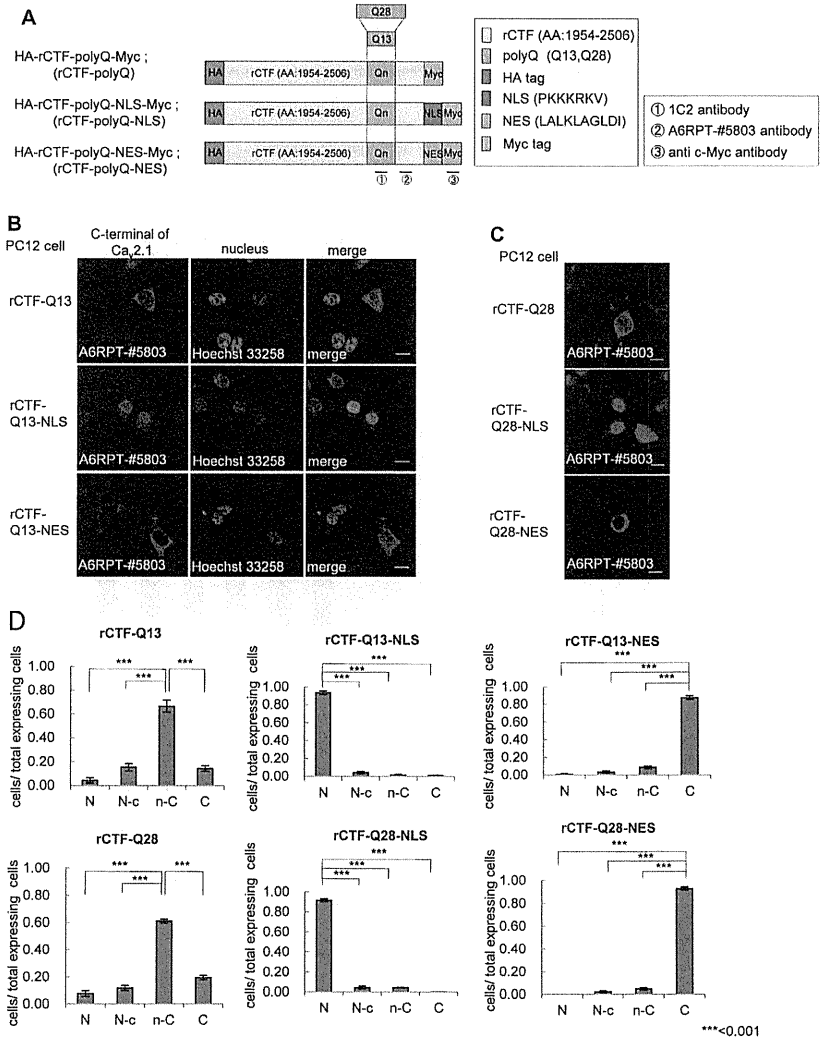

Figure 1. Localization signals efficiently change the intracellular location of CTF. (A) Recombinant $Ca_v2.1$ C-terminal fragment (rCTF)s used in this study. Definition of rCTF (amino acid(AA) #1954–2506 in $Ca_v2.1$ [GenBank AB035726] [18]), artificial nuclear localization or export signals (NLS or NES), two different polyglutamine (Qn) (Q13; Q28) and recognition sites of three different antibodies (1C2 against expanded polyQ, A6RPT-#5803 against $Ca_v2.1$ CTF, c-Myc antibody against Myc-tag) are shown. (B) The rCTF-Q13 is predominantly expressed in the cytoplasm of PC12 cells. The NLS and NES efficiently localize the tagged rCTF to the designed location [A6RPT-#5803 antibody (red), Hoechst 33258 (blue)] (scale bar: 10 μm). (C) The NLS and NES efficiently shift rCTFs with expanded polyQ (Q28) into the nucleus and cytoplasm respectively (scale bars: 10 μm). (D) The proportion of the subcellular localization in each rCTF expressed. The rCTF-polyQ is predominantly, though not exclusively, expressed in the cytoplasm of PC12 cells. The localization signals change subcellular localization of rCTFs-polyQ effectively. (N; the cells expressing rCTF exclusively in the nucleus; N-c: the cells expressing rCTF predominantly in the nucleus than in the cytoplasm; n-C: the cells expressing rCTF predominantly in the cytoplasm than in the nucleus; C: the cells expressing rCTF exclusively in the cytoplasm) (For D: ***:p<0.001;ANOVA. Error bars indicate ± SEM.).
doi:10.1371/journal.pone.0050121.g001

started to be detected on Day4 and become conspicuous on Day6 (Figure 2E). In stable rCTF-Q13-NES cells, the rCTF aggregates were observed only with A6RPT-#5803 but not with 1C2. Because no aggregates are detected by A6RPT-#5803 in normal human brains, the stable PC12 cells expressing rCTF-Q13-NES can be considered as an exaggerated cell model for normal CTF. On the other hand, those expressing rCTF-Q28-NES recapitulated SCA6 aggregates in human Purkinje cells, showing A6RPT-#5803 and 1C2 double-positive aggregates [18].

Cytoplasmic expression of CTF triggered cell death with aggregate formation

We next asked whether the CTF is more toxic in the nucleus than in the cytoplasm, as in other polyQ diseases [2]. To address this question, we transiently over-expressed rCTF-polyQ-NLS or rCTF-polyQ-NES in HEK293T cells, and measured cell death by lactate dehydrogenase (LDH) assay at 72 hours after transfection. Surprisingly, we found that the rCTF-polyQ-NES showed stronger toxicity than the rCTF-polyQ-NLS, regardless of the polyQ lengths (Figure 3A). This is striking, as most proteins

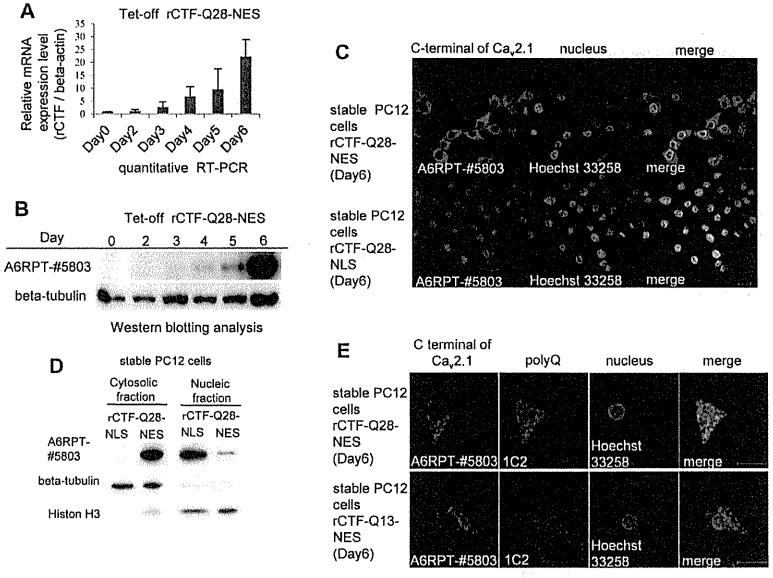

Figure 2. Characterization of inducible PC12 cells stably expressing rCTFs. Only the cell lines expressing rCTF-Q28-NES, rCTF-Q28-NLS and rCTF-Q13-NES are shown here (*Other cells are shown upon request*). (A) A timeline of rCTF expression in PC12 cells stably expressing rCTF-Q28-NES by quantitative real-time PCR (qRT-PCR). The rCTF mRNA level starts to be detected inDay3 and gradually increases with a time-dependent manner. The beta-actin expression level was used as an internal control. (B) A timeline of rCTF expression in PC12 cells stably expressing rCTF-Q28-NES by Western blot using the A6RPT-#5803 antibody. Protein expression starts to be detected on the fourth day after the Dox removal ("Day4") and reaches abundant level in Day6. Anti beta-tubulin antibody was used as internal control. (C) Immunofluorescence cytochemistry in Day6 stable PC12 cell lines expressing rCTF-Q28-NES (upper row) and rCTF-Q28-NLS (lower row). The NES-tag faithfully anchored rCTF to the cytoplasm, whereas the NLS-tag efficiently directed rCTF to the nucleus. (D) Western blot analysis on protein extracts from stable cell lines expressing rCTF-Q28-NLS and rCTF-Q28-NES confirming efficient intracellular localizations (A6RPT-#5803: anti-$Ca_v2.1$CTF, beta-tubulin: a cytoplasmic protein marker, Histone H3: a nuclear protein marker). (E) Immunofluorescence cytochemistry in Day6 stable PC12 cell lines expressing rCTF-Q28-NES (upper row) and rCTF-Q13-NES (lower row). In PC12 cells expressing rCTF-Q28-NES, cytoplasmic aggregates are detected by both A6RPT-#5803 and 1C2. In rCTF-Q13-NES cells, rCTF-aggregates are recognized by the anti-$Ca_v2.1$ antibody A6RPT-#5803, but not by 1C2, a monoclonal antibody specific for expanded polyQ. (For C&E, scale bars: 10 μm).
doi:10.1371/journal.pone.0050121.g002

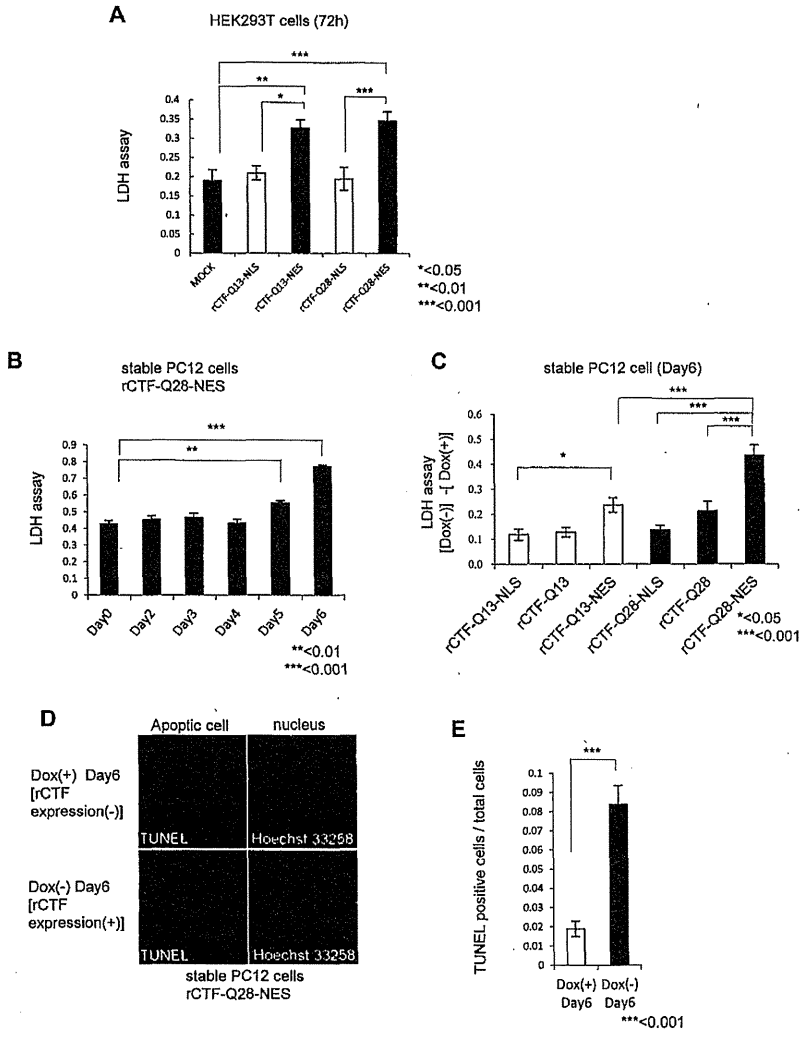

Figure 3. The rCTF is toxic to cells when expressed in the cytoplasm. (A) Cell death in transiently over-expressed HEK293T cells assessed by LDH level at 72 hours after transfection. The rCTF-polyQ-NES exhibits stronger cytotoxicity than rCTF-polyQ-NLS. (B) Time course of cell death in inducible rCTF-Q28-NES PC12 cell line. Cell toxicity is detected from Day5 and become prominent in Day6. (C) The cell death at Day6 compared in 6 inducible PC12 cell lines (rCTF-Q13, rCTF-Q13-NLS, rCTF-Q13-NES, rCTF-Q28, rCTF-Q28-NLS, rCTF-Q28-NES). The cell line expressing rCTF-Q28-NES exerts the strongest cell death. Y-axis shows differences of LDH values between (Dox(−)) and (Dox(+)) states. Cells do not show obvious cell death in Dox(+) states. (D&E) TUNEL positive cells are dramatically increased when doxycyclin is removed (Dox(−)). Eight randomly selected microscope fields were counted for TUNEL positive cells and total cell numbers. (For A to C and E: *: p<0.05; **: p<0.01; ***:p<0.001;ANOVA for A to C. Mann-Whitney's U test for E. Error bars indicate ± SEM.).
doi:10.1371/journal.pone.0050121.g003

causing polyQ diseases show dramatic cell death when they are expressed in the nucleus.

We then compared the cell toxicity for the period after the Dox removal. In the inducible stable PC12 cell line expressing the rCTF-Q28-NES, we found that the cell death measured by LDH assay started to appear on Day5, and become prominent on Day6 (Figure 3B). We also found the cell death is not seen when the Dox is kept in the media, confirming that the cell death is induced by the rCTF expression in the cytoplasm. Based on these results, we compared cell death at Day6 in the 6 stable PC12 cell lines. In a manner consistent with results from transient expression in HEK293T cells, we found that the stable PC12 cells expressing rCTF-polyQ(Q13, Q28)-NES exerted stronger toxicity than rCTF-polyQ(Q13, Q28) or rCTF-polyQ(Q13, Q28)-NLS (Figure 3C). Importantly, we also found that the PC12 cells expressing rCTF-Q28-NES revealed the strongest toxicity among the 6 cell lines. This is an intriguing finding demonstrating that such a small polyQ repeat, the length that corresponds to a normal repeat in other polyQ diseases, exerts toxicity in the cytoplasm of cultured cells. The cell death was compatible with apoptosis and showed a significant increase of TUNEL (TdT-mediated dUTP-biotin nick end labeling)-positive cells (Figure 3D & 3E).

The cytoplasmic $Ca_v2.1$-CTF aggregates co-localize with CREB and phosphorylated(p)-CREB resulting in reductions of CREB/p-CREB in the nuclei

In other polyQ diseases such as HD, one of the underlying mechanisms for suppressing CREB-dependent transcription is the sequestration of CREB-binding protein (CBP) by the aggregations of mutant proteins within the nuclei [22–25]. However, it is not known if this is also the case in SCA6. To clarify whether and how the CTF suppresses CREB-dependent transcription, we analyzed localizations of rCTF, CREB and phosphorylated-CREB (p-CREB), the active form of CREB, in PC12 cell models. While the immunoreactivities for CREB and p-CREB were both strong in the nuclei, they were very weak in the cytoplasm of non-transfected PC12 cells (Figure 4A). On the other hand, in PC12 cells transiently expressing rCTF-Q28-NES, we found that the cytoplasmic rCTF aggregates co-localized with both CREB and p-CREB demonstrating focally strong immunoreactivities for these proteins (Figure 4B). Similar co-localizations were also observed both for CREB and p-CREB with rCTF aggregates in the stable PC12 cell lines expressing rCTF-Q28-NES in contrast to the control Dox(+) cells (Figure 4C & 4D). When rCTF-Q13-NES was transiently over-expressed in PC12 cells, CREB and p-CREB also co-localized with rCTF aggregates in the cytoplasm (Figure S3). These results suggested to us that the rCTF expression in the cytoplasm indeed alters intracellular distribution of CREB and p-CREB irrespective of the polyQ length.

We also examined whether the formation of cytoplasmic rCTF aggregates influence the quantity of CREB and p-CREB in the nucleus. By Western blot analysis, we found that they were both decreased when the rCTF was expressed in the cytoplasm (Figure 4E). Surprisingly, the reductions of CREB and p-CREB in the nucleus were not observed when the rCTF was expressed directly in the nucleus. Therefore, over-expressing the rCTF in the cytoplasm leads to the reductions of CREB and p-CREB in the nuclei, possibly by retaining them in the cytoplasm through their co-localization with the CTF aggregates. This also suggests that the cytoplasmic CTF aggregates cause the repression of the CREB-dependent transcription through abnormal intracellular trafficking of CREB.

CREB co-localized with cytoplasmic aggregates in the human SCA6 Purkinje cells

We finally examined whether the CREB co-localizes with $Ca_v2.1$ microscopic aggregates in SCA6 Purkinje cells. Although CREB expression was seen in the nuclei of cultured cells, the immunoreactivity against CREB was present but weak and homogeneous in the neuronal cytoplasm in control human Purkinje cells (Figure 5A). This would indicate species or cellular differences in the immunoreactivity against the antibody we used. In SCA6 human Purkinje cells, CREB immunoreactivity was also seen expressed in the cytoplasm. However, granular or thread-like CREB-immunoreactive structures were frequently observed in the cytoplasm of SCA6 Purkinje cells (Figure 5B). When these structures were counted, we observed that SCA6 Purkinje cells show a higher number of CREB-immunoreactive structures than controls (Figure 5 C). We next examined the relationship between the CREB and 1C2-immunoreactive $Ca_v2.1$ aggregates in the SCA6 Purkinje cells by double immunofluorescence technique. We found that the 1C2-immunoreactive microscopic polyQ aggregates in the cytoplasm of SCA6 Purkinje cells indeed co-localize with CREB (Figure 5D). Among the remaining Purkinje cells in the three SCA6 cerebella, we found that 50% of such Purkinje cells had the co-localization of CREB and $Ca_v2.1$ aggregates. As there are no $Ca_v2.1$ aggregates in control Purkinje cells, such co-localization is specific to SCA6 Purkinje cells (Figure 5 E). Also, this co-localization mimics what we observed in cultured cells, suggesting that altered intracellular trafficking of CREB takes place in human SCA6 Purkinje cell as well.

Discussion

Molecular genetics of SCA6 are characterized by two main features; namely, 1) a small polyQ expansion (normal range 4–19 repeat *vs* SCA6 20–33 repeat) that falls within a normal range of other polyQ diseases (usually more than 35 repeat in other polyQ diseases), and 2) the cytoplasmic localization of aggregations which contrasts with nuclear localization in other polyQ diseases [2,16,17]. It should be noted that nuclear aggregates were seen in SCA6 Purkinje cells in a very small amount, though cytoplasmic aggregations are far dominant in both immunohistochemical and Western blotting observations [18]. Thus, it remained to be clarified whether cytoplasmic aggregates are more toxic than nuclear ones, or *vice versa* as in other polyQ diseases. To define which location of the CTF is more toxic, and also to elucidate the mechanisms of its toxicity, we developed cell models expressing rCTF tagged with either NLS or NES. These signals faithfully targeted the rCTF to the aimed intracellular cites (cytoplasm or nucleus). We here demonstrate that the rCTF-Q13 and -Q28 both consistently show toxicity in cultured HEK293T and PC12 cells when the rCTFs are expressed in the cytoplasm. On the other hand, neither rCTF-Q13 nor rCTF-Q28 showed obvious toxicity when expressed in the nucleus. Furthermore, the toxicity exerted by rCTF-Q28-NES was more profound than that of rCTF-Q13-NES, an important observation supporting the fundamental idea that SCA6 complies with the general rule of polyQ-length dependent toxicity in all polyQ diseases. Taking these observations

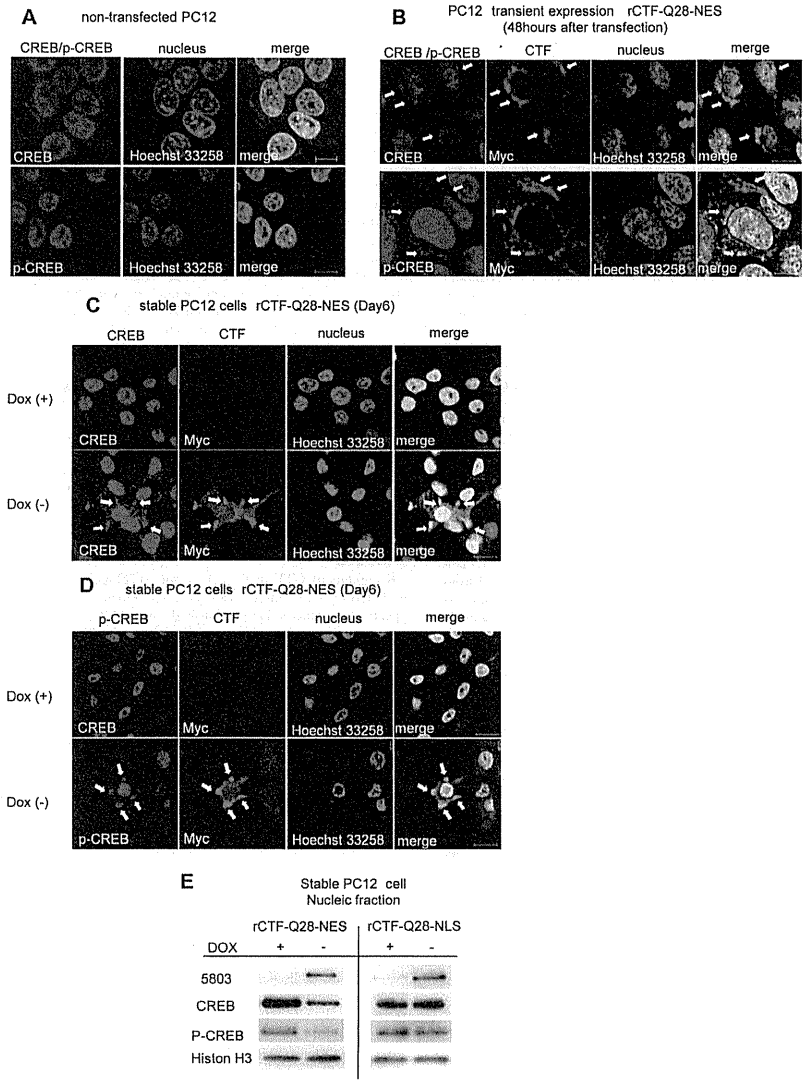

Figure 4. CREB co-localizes with intracytoplasmic CTF aggregates and quantity of CREB is decreased in cultured cell model. (A) In non-transfected PC12 cells, CREB and p-CREB-immunofluorescence labeling is strong in the nucleus, while the cytoplasm shows only weak and diffuse immunofluorescence. (B) In PC12 cells over-expressing rCTF-Q28-NES, the cytoplasmic CTF aggregates co-localize with CREB (*upper row*) and p-CREB (*lower row*), showing focally strong immunofluorescence in their cell bodies (arrows). (C&D) In contrast to the Dox(+) stable PC12 cells (upper row in C&D), co-localizations of CREB (*lower row in C*) or p-CREB (lower row in D) with cytoplasmic aggregates are also observed in Dox(−) stable PC12 cells expressing rCTF-Q28-NES (arrows). (E) The quantities of CREB and p-CREB in the nucleus were both decreased when the rCTF was expressed in the cytoplasm, but not so when the rCTF was targeted in the nucleus. (For A-D: scale bars: 10 μm).
doi:10.1371/journal.pone.0050121.g004

together, it seems rational to consider that important cascades in SCA6 pathogenesis occur in the cytoplasm of CTF-expressing cells, such as Purkinje cells.

Then how does the CTF cause cell death? Although this is still an open question, we here showed that the cytoplasmic overexpression of rCTF resulted in the altered intracellular distributions of CREB and p-CREB. The CREB and p-CREB both co-localized with $Ca_v2.1$-CTF aggregates in the cytoplasm, and the amount of CREB and p-CREB were both reduced in the nuclei of cultured cells. Furthermore, co-localization of CREB and cytoplasmic $Ca_v2.1$ aggregates was confirmed in human SCA6 Purkinje cells, suggesting that the suppression of CREB-mediated transcription takes place in SCA6 Purkinje cells. Indeed, we recently found that the brain derived neurotrophic factor (BDNF) mRNA, which is regulated by the CREB-mediated transcription, is reduced in SCA6 human cerebellum [26]. It is also important to note that the CREB and p-CREB were not reduced even when the rCTF was over-expressed in the nuclei by tagging the rCTF with NLS. Although the present observation is strikingly different than with other polyQ diseases, in which suppression of CREB-transcription is seen by nuclear localizations of mutated proteins [23,24,27], it should be noted that polyQ-aggregates are also seen in the cytoplasm in other polyQ diseases such as HD [28] and MJD [13], raising a hypothesis that CREB-transcriptional repression may be further enhanced by the formation of protein aggregates in the cytoplasm. It has been shown that the CREB is transported from axons to cell body [29], and translocated from the cytoplasm to the nucleus [30,31]. This retrograde trafficking has been claimed to be important for neurons to survive. Thus, it may be possible that the cytoplasmic protein aggregates can affect neuronal survival by trapping the CREB in the cytoplasm resulting in the reductions of the nuclear CREB and pCREB levels. Interestingly, the CREB-related transcription is suppressed in Parkinson's disease by the formation of p-CREB aggregates in the neuronal cytoplasm [31]. However, many issues remain unsolved concerning the link between the $Ca_v2.1$ with expanded polyQ and the suppression of the CREB-related transcription. For example, it is not known whether the CTF could directly bind CREB/pCREB, as we failed to detect direct interactions between rCTF and CREB by co-immunoprecipitation experiments (data not shown). It is thus possible that some other proteins mediate co-localization of $Ca_v2.1$ aggregates and CREB/pCREB. Further studies are needed to elucidate how CREB and p-CREB co-localize with $Ca_v2.1$ aggregates.

Our observation of cytoplasmic toxicity of the CTF is confounded by two previous studies showing rCTF toxicity in the nuclei [19,20], However, as we showed here, tagging rCTF with EGFP may artificially confine the rCTF into the nuclei. It should also be noted that the components of the rCTFs are not exactly the same as the four studies [18–21]: the present study utilized CTF (Amino acids #1954–#2506) [18] which is exactly the same with the one Li et al. used [20], except for the differences in tag proteins. The CTF used by Kordasiewicz HB et al. (Amino acids #2096–#2510) [19]is slightly shorter than ours, and Marquèze-Pouey et al. [21]used a much shorter CTF (corresponding amino acids #2319-C-term of rat $Ca_v2.1$). Of note is that the size of rCTF we used here is very close to the native CTF judging from the result in Western blot [18]. The toxicity when expressed in the cytoplasm is also supported by another study showing that the rCTF with expanded polyQ caused cell death and promoted the CTF to be condensed at the plasma membrane by interacting with myosin IIB [21]. Although the rCTF-Q28-NLS was not obviously toxic in our system, we do not preclude a possibility that the CTF in the nucleus could exert subtle toxicity. Since the CTF is also present in the nucleus in the SCA6 human brains, the true pathogenic mechanisms of SCA6 are predicted to be more complicated than our cellular models. Particularly, we must admit that our cultured cells should have different intracellular conditions and thus should respond differently to various stimuli compared to the Purkinje cells. Nevertheless, we consider that tracking downstream events in each location of CTF would be an important step for exploring the disease mechanism.

In conclusion, we showed that the CTF with a small polyQ expansion is sufficient to cause toxicity when it forms aggregates in the cytoplasm. This was associated with changes in CREB/p-CREB intracellular distribution, and their quantities in the nucleus. A precise understanding of the consequences of intracellular CTF aggregations such as the mechanism of CREB inactivation and the downstream gene expression changes appear important for establishing fundamental therapy of SCA6.

Materials and Methods

Constructs

Recombinant CTF of $Ca_v2.1$ vector (rCTF-polyQ) encoding the C-terminal 553 amino acids (AA) with either 13 or 28 CAG repeats was constructed as previously described [6]. NLS and NES tags were generated from custom oligonucleotides (Sigma-Aldrich Japan, Tokyo, Japan). NLS was derived from SV40 large T antigen (PKKKRKV) and NES was derived from human cAMP-dependent protein kinase inhibitor, alpha form (LALKLAGLDI), and flanked by restriction sites of *Xba*I. The rCTF-polyQ constructs were digested with *Eco*RV and *Pme*I, destroying the *Xba*I restriction site in the multi cloning site. Then, the resulting blunt-end fragment of rCTF-polyQ was ligated into the *Pme*I-digested pcDNA3.1 (Invitrogen, CA, USA). Finally, NLS or NES was cloned into the *Xba*I site of rCTF-polyQ in pcDNA3.1. EGFP fused rCTF vectors were constructed with pEGFP-C2 vectors (Clontech, CA, USA). The rCTF-polyQ constructs were digested with *Bgl*II and *Eco*RV and the resulting fragment of rCTF-polyQ was ligated into EGFP-C2 vector digested with *Bgl*II and *Sma*I in multi cloning site.

Cell culture and transfection of genes-of-interest

Rat adrenal pheochromocytoma PC12 cells and Human embryonic kidney (HEK293T) cells were obtained from American Type Culture Collection (ATCC, VA, USA). PC12 cells were grown in Dulbecco's Modified Eagle's Medium (DMEM) (WAKO, Saitama, Japan) containing 10% horse serum (HS) (GIBCO, Tokyo, Japan), 5% fetal bovine serum (FBS) (GIBCO) and 1% penicillin/streptomycin (PS) (GIBCO) in a humidified atmosphere of 5% CO_2 at 37°C. HEK293T cells were grown in DMEM containing 10% FBS and 1% PS in a humidified atmosphere of 5% CO_2 at 37°C. Cells were transfected using Lipofectamine 2000 (Invitrogen) according to the manufacturer's protocol.

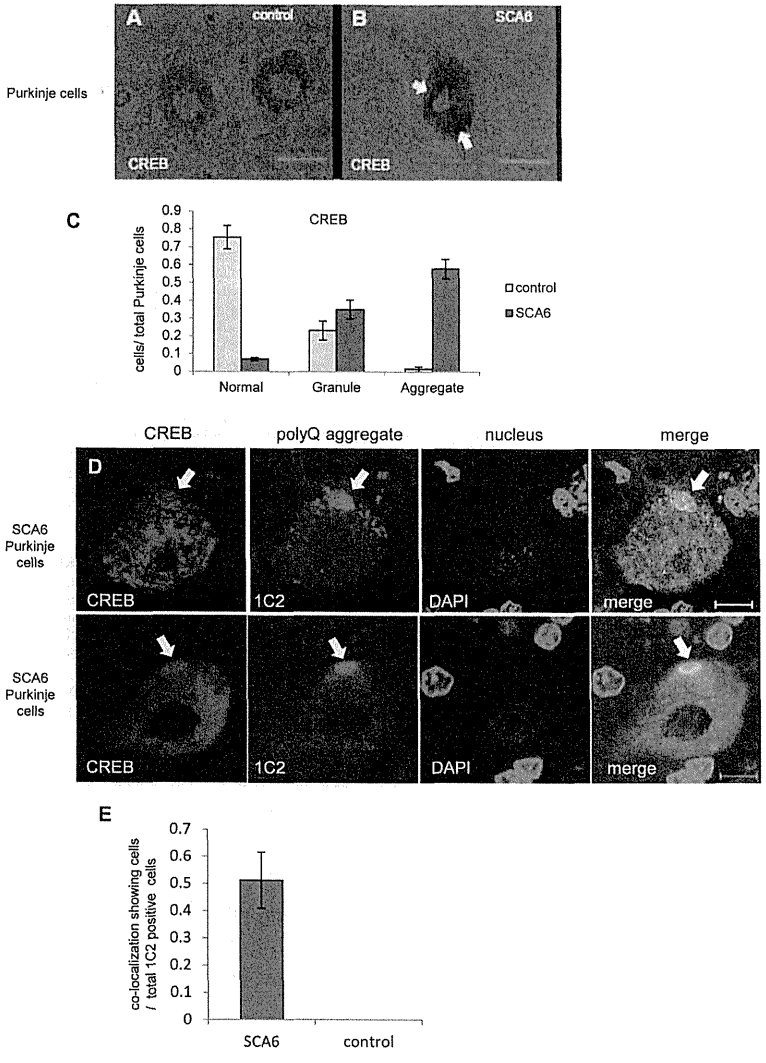

Figure 5. CREB and $Ca_v2.1$ aggregates co-localize in SCA6 human Purkinje cells. (A) In a control brain affected with Parkinson's disease, the immunoreactivity against CREB is present but weak and homogeneous in the neuronal cytoplasm of two Purkinje cells. (B) In SCA6 human Purkinje cells, focally accentuated immunoreactive structures (arrows) are seen in the cytoplasm. (C) In ten control brains, a vast majority of Purkinje cells showed weak and diffuse immunoreactivity for the anti-CREB antibody as demonstrated in the Figure 5 A. In contrast, aggregate-like CREB-immunoreactive structures were seen in the Purkinje cells from three SCA6 cerebella. *Please refer to the Materials and Methods for the detailed description on the criteria of CREB-immunoreactivities.* (D) On double immunofluorescence analysis using a rabbit polyclonal CREB antibody and 1C2, a mouse monoclonal antibody against expanded polyQ tracts, microscopic $Ca_v2.1$ aggregates in the cytoplasm of the SCA6 Purkinje cells indeed co-localized with CREB (arrows). (For A&B: scale bars: 50 μm; for D&E: scale bar: 10 μm). (E) In three SCA6 cerebella, approximately 50% of Purkinje cells containing 1C2-positive polyQ aggregates in the cytoplasm showed co-localization of the polyQ aggregates and CREB. In contrast, the Purkinje cells in control cerebella did not show 1C2-positive aggregates resulting in no co-localizations.
doi:10.1371/journal.pone.0050121.g005

Generation and culture of inducible PC12 stable cell lines

PC12 Tet-off cell lines (Clontech, CA, USA) were grown in DMEM containing 10% HS, 5% TET-system approved FBS (Clontech), 1% PS and 200 μg/ml G418 (SIGMA, Tokyo, Japan) in a humidified atmosphere of 5% CO_2 at 37°C. Tet-off PC12 cells were transfected with each rCTF vector at 70% confluence using Lipofectamine 2000 (Invitrogen). Positive clones were selected in complete medium containing 200 μg/ml G418 (SIGMA), 200 μg/ml hygromycin (WAKO) and 2 μg/ml doxycycline (Dox) (Clontech). To initiate differentiation, cells were plated on collagen type I-coated plate (IWAKI, Tokyo, Japan) and grown in DMEM containing 1% HS, 1% PS, 200 μg/ml G418, 200 μg/ml hygromycin, 2 μg/ml Dox and 50 ng/ml nerve growth factor (NGF) 2.5S (Invitrogen, CA, USA).

Immunoblot analysis

The procedure was described previously [18]. Subcellular fractionation was performed with NE-PER Nuclear and Cytoplasmic Extraction Reagents (Pierce, IL, USA).

Cell toxicity and viability analysis

Cell toxicity were assessed by lactate dehydrogenase (LDH) assay with CytoTox 96® Non-Radioactive Cytotoxicity Assay (Promega, WI, USA) and TUNEL assay with DeadEnd™ Fluorometric TUNEL System (Promega). Cell toxicity with LDH assay was calculated using the following formula (experimental LDH release/maximum LDH release).

Immunocytochemistry

The procedure was described previously [6,18]. Either of the following primary antibodies was used; mouse monoclonal anti-c-Myc antibody (diluted with phosphate buffered saline (PBS) into 1:100) (Santa Cruz Biotechnology, CA, USA), rabbit polyclonal A6RPT-#5803 (1:500), rabbit polyclonal anti-CREB antibody (1:500) (Cell Signaling Technology, MA, USA), rabbit polyclonal anti-p-CREB antibody (1:100) (Cell Signaling Technology), mouse monoclonal anti-expanded 1C2 (1:1000)(Millipore, CA, USA). To visualize the anti-p-CREB antibody signal, endogenous PKA was activated by the 10 μM forskolin containing medium for 1 hour before the fixation.

To examine the proportion of cells with a particular subcellular localization of each rCTF, the cells expressing each rCTF were classified into the following four groups and counted in five randomly selected microscope fields: N; the cells expressing rCTF exclusively in the nucleus; N-c: the cells expressing rCTF predominantly in the nucleus than in the cytoplasm; n-C: the cells expressing rCTF predominantly in the cytoplasm than in the nucleus; C: the cells expressing rCTF exclusively in the cytoplasm. The proportion of subcellular localization was calculated using the following formula: total number of cells in each of the four groups/ total rCTF expressing cells. The difference was then statistically analyzed using ANOVA.

Immunohistochemistry

Formalin-fixed paraffin-embedded tissue sections of the cerebellar cortex were analyzed. Three SCA6 brains and 10 controls (4 individuals with Parkinson's disease, 2 with amyotrophic lateral sclerosis, 2 with multiple system atrophy, 1 with cerebral infarction, and 1 with SCA31) were investigated. The procedure was described previously [6,13,18]. Either of the following primary antibodies was used; A6RPT-#5803 (diluted in 1:500 concentration with PBS), 1C2 (1:1000), and anti-CREB antibody (1:100). For double immunofluorescent labeling, sections were incubated with 1% sudan black B in 70% methanol for 5 minutes to block the autofluorescence.

To examine the proportion of Purkinje cells which shows different immunostaining against CREB, five random microscopic fields were selected and each immunostained Purkinje cell was classified into the following three categories; "Normal": the Purkinje cells which were stained diffusely in the cytoplasm; "Granule": the Purkinje cells containing small puncta in the cytoplasm; "Aggregate": the Purkinje cells showing thread-like structures or coarse large aggregates in the cytoplasm. The proportion of each category was calculated using the following formula: the number of Purkinje cell in each of the three groups/ total number of immunostained Purkinje cells.

To examine the proportion of Purkinje cells which shows co-localization of CREB and 1C2 positive aggregates, ten consecutive Purkinje cells containing 1C2 positive aggregates in the cytoplasm was examined under a confocal laser microscope in three different regions of cerebellar cortex and calculated.

RNA isolation and real time quantitative PCR (RT-qPCR)

Total cellular RNA was isolated by TRIzol (Invitrogen, CA, USA) according to the manufactures' protocol. Cellular extracts were then treated with DNase (Invitrogen) and total RNA was quantified on a Nanodrop spectrophotometer. Total RNA was carried out reverse transcription to cDNA using a super script® III first-strand synthesis system for RT-PCR (Invitrogen) and random hexamers. The primer and probes for rCTF was designed from Life technologies (Applied biosystems by Life technologies, CA, USA). The other primer and probes were from TaqMan® Gene Expression Assays.

Statistical analysis

Where applicable, data are presented as mean ±standard error of the mean (SEM), and statistical analysis was tested by using Mann-Whitney's U test (for TUNEL assay) or a one-way analysis of variance (ANOVA) tests (all assays except for TUNEL assay). Each experiment was repeated three times independently and statistical analysis was performed.

Supporting Information

Figure S1 Presence of enhanced green fluorescent protein (EGFP) dramatically shifts the tagged rCTF into the nuclei. (A) A scheme of the recombinant $Ca_v2.1$ C-terminal fragment (rCTF) vectors with or without EGFP used in this study. (B) The rCTF-polyQ (either Q13 or Q28)-EGFP locates almost exclusively in the nuclei irrespective of the length of polyQ. This localization is quite different from the predominantly cytoplasmic location of rCTF-polyQ without EGFP. (scale bars: 50 μm) (C) The proportion of the subcellular localization of each rCTF in the transiently expressing PC12 cells. (N; the cells expressing rCTF exclusively in the nucleus; N-c: the cells expressing rCTF predominantly in the nucleus than in the cytoplasm; n-C: the cells expressing rCTF

predominantly in the cytoplasm than in the nucleus; C: the cells expressing rCTF exclusively in the cytoplasm).
(PPTX)

Figure S2 rCTF expression in HEK293T cells. While rCTF-Q13 distributed both in the cytoplasm and nucleus of HEK293T cells, NLS and NES both efficiently shifted the rCTF localization in the nucleus and cytoplasm, respectively. (scale bars: 10μm).
(PPTX)

Figure S3 Co-localization of CREB and p-CREB with cytoplasmic aggregates in rCTFQ13-NES expressing PC12 cells. In PC12 cells over-expressing rCTF-Q13-NES, some of the cytoplasmic CTF aggregates co-localized with CREB (upper row) and p-CREB (lower row) (co-localizations: arrows).
(PPTX)

References

1. Orr HT, Zoghbi HY (2007) Trinucleotide repeat disorders. Annu Rev Neurosci 30: 575–621.
2. Shao J, Diamond MI (2007) Polyglutamine diseases: emerging concepts in pathogenesis and therapy. Hum Mol Genet 16 Spec No. 2: R115–123.
3. Zhuchenko O, Bailey J, Bonnen P, Ashizawa T, Stockton DW, et al. (1997) Autosomal dominant cerebellar ataxia (SCA6) associated with small polyglutamine expansions in the alpha 1A-voltage-dependent calcium channel. Nat Genet 15: 62–69.
4. Ishikawa K, Tanaka H, Saito M, Ohkoshi N, Fujita T, et al. (1997) Japanese families with autosomal dominant pure cerebellar ataxia map to chromosome 19p13.1-p13.2 and are strongly associated with mild CAG expansions in the spinocerebellar ataxia type 6 gene in chromosome 19p13.1. Am J Hum Genet 61: 336–346.
5. Gomez CM, Thompson RM, Gammack JT, Perlman SL, Dobyns WB, et al. (1997) Spinocerebellar ataxia type 6: gaze-evoked and vertical nystagmus, Purkinje cell degeneration, and variable age of onset. Ann Neurol 42: 933–950.
6. Ishikawa K, Fujigasaki H, Saegusa H, Ohwada K, Fujita T, et al. (1999) Abundant expression and cytoplasmic aggregations of [alpha]1A voltage-dependent calcium channel protein associated with neurodegeneration in spinocerebellar ataxia type 6. Hum Mol Genet 8: 1185–1193.
7. Matsuyama Z, Wakamori M, Mori Y, Kawakami H, Nakamura S, et al. (1999) Direct alteration of the P/Q-type Ca2+ channel property by polyglutamine expansion in spinocerebellar ataxia 6. J Neurosci 19: RC14.
8. Toru S, Murakoshi T, Ishikawa K, Saegusa H, Fujigasaki H, et al. (2000) Spinocerebellar ataxia type 6 mutation alters P-type calcium channel function. J Biol Chem 275: 10893–10898.
9. Restituito S, Thompson RM, Eliet J, Raike RS, Riedl M, et al. (2000) The polyglutamine expansion in spinocerebellar ataxia type 6 causes a beta subunit-specific enhanced activation of P/Q-type calcium channels in Xenopus oocytes. J Neurosci 20: 6394–6403.
10. Piedras-Renteria ES, Watase K, Harata N, Zhuchenko O, Zoghbi HY, et al. (2001) Increased expression of alpha 1A Ca2+ channel currents arising from expanded trinucleotide repeats in spinocerebellar ataxia type 6. J Neurosci 21: 9185–9193.
11. Saegusa H, Wakamori M, Matsuda Y, Wang J, Mori Y, et al. (2007) Properties of human Cav2.1 channel with a spinocerebellar ataxia type 6 mutation expressed in Purkinje cells. Mol Cell Neurosci 34: 261–270.
12. Watase K, Barrett CF, Miyazaki T, Ishiguro T, Ishikawa K, et al. (2008) Spinocerebellar ataxia type 6 knockin mice develop a progressive neuronal dysfunction with age-dependent accumulation of mutant CaV2.1 channels. Proc Natl Acad Sci U S A 105: 11987–11992.
13. Ishikawa K, Owada K, Ishida K, Fujigasaki H, Shun Li M, et al. (2001) Cytoplasmic and nuclear polyglutamine aggregates in SCA6 Purkinje cells. Neurology 56: 1753–1756.
14. Yabe I, Sasaki H, Matsuura T, Takada A, Wakisaka A, et al. (1998) SCA6 mutation analysis in a large cohort of the Japanese patients with late-onset pure cerebellar ataxia. J Neurol Sci 156: 89–95.
15. Takahashi H, Ishikawa K, Tsutsumi T, Fujigasaki H, Kawata A, et al. (2004) A clinical and genetic study in a large cohort of patients with spinocerebellar ataxia type 6. J Hum Genet 49: 256–264.
16. DiFiglia M, Sapp E, Chase KO, Davies SW, Bates GP, et al. (1997) Aggregation of huntingtin in neuronal intranuclear inclusions and dystrophic neurites in brain. Science 277: 1990–1993.
17. Paulson HL, Perez MK, Trottier Y, Trojanowski JQ, Subramony SH, et al. (1997) Intranuclear inclusions of expanded polyglutamine protein in spinocerebellar ataxia type 3. Neuron 19: 333–344.
18. Ishiguro T, Ishikawa K, Takahashi M, Obayashi M, Amino T, et al. (2010) The carboxy-terminal fragment of alpha(1A) calcium channel preferentially aggregates in the cytoplasm of human spinocerebellar ataxia type 6 Purkinje cells. Acta Neuropathol 119: 447–464.
19. Kordasiewicz HB, Thompson RM, Clark HB, Gomez CM (2006) C-termini of P/Q-type Ca2+ channel alpha1A subunits translocate to nuclei and promote polyglutamine-mediated toxicity. Hum Mol Genet 15: 1587–1599.
20. Li L, Saegusa H, Tanabe T (2009) Deficit of heat shock transcription factor 1-heat shock 70 kDa protein 1A axis determines the cell death vulnerability in a model of spinocerebellar ataxia type 6. Genes Cells 14: 1253–1269.
21. Marqueze-Pouey B, Martin-Moutot N, Sakkou-Norton M, Leveque C, Ji Y, et al. (2008) Toxicity and endocytosis of spinocerebellar ataxia type 6 polyglutamine domains: role of myosin IIb. Traffic 9: 1088–1100.
22. Shimohata T, Nakajima T, Yamada M, Uchida C, Onodera O, et al. (2000) Expanded polyglutamine stretches interact with TAFII130, interfering with CREB-dependent transcription. Nat Genet 26: 29–36.
23. McCampbell A, Taylor JP, Taye AA, Robitschek J, Li M, et al. (2000) CREB-binding protein sequestration by expanded polyglutamine. Hum Mol Genet 9: 2197–2202.
24. Nucifora FC, Jr., Sasaki M, Peters MF, Huang H, Cooper JK, et al. (2001) Interference by huntingtin and atrophin-1 with cbp-mediated transcription leading to cellular toxicity. Science 291: 2423–2428.
25. Milnerwood AJ, Gladding CM, Pouladi MA, Kaufman AM, Hines RM, et al. (2010) Early increase in extrasynaptic NMDA receptor signaling and expression contributes to phenotype onset in Huntington's disease mice. Neuron 65: 178–190.
26. Takahashi M, Ishikawa K, Sato N, Obayashi M, Niimi Y, et al. (2012) Reduced brain-derived neurotrophic factor (BDNF) mRNA expression and presence of BDNF-immunoreactive granules in the spinocerebellar ataxia type 6 (SCA6) cerebellum. Neuropathology. In press.
27. Jiang H, Nucifora FC, Jr., Ross CA, DeFranco DB (2003) Cell death triggered by polyglutamine-expanded huntingtin in a neuronal cell line is associated with degradation of CREB-binding protein. Hum Mol Genet 12: 1–12.
28. Li XJ (1999) The early cellular pathology of Huntington's disease. Mol Neurobiol 20: 111–124.
29. Cox LJ, Hengst U, Gurskaya NG, Lukyanov KA, Jaffrey SR (2008) Intra-axonal translation and retrograde trafficking of CREB promotes neuronal survival. Nat Cell Biol 10: 149–159.
30. Forwood JK, Lam MH, Jans DA (2001) Nuclear import of Creb and AP-1 transcription factors requires importin-beta 1 and Ran but is independent of importin-alpha. Biochemistry 40: 5208–5217.
31. Chalovich EM, Zhu JH, Caltagarone J, Bowser R, Chu CT (2006) Functional repression of cAMP response element in 6-hydroxydopamine-treated neuronal cells. J Biol Chem 281: 17870–17881.

Acknowledgments

The authors thank Professor Hirotsugu Asahara, Dr. Kei Watase and Mr. Toshiki Unno (Tokyo Medical and Dental University) for their stimulating discussions and technical advice, Mr. Ando and Mrs. Matsuo for their excellent technical assistance, and Scientific Language Editing Team, Tsukuba, Japan, for proofreading the manuscript for editing English.

Author Contributions

Conceived and designed the experiments: KI MT. Performed the experiments: MT MO TI NS YN KO KM YM. Analyzed the data: MT KM YM H. Tanaka. Contributed reagents/materials/analysis tools: FT RD MY H. Takahashi TK OM YE. Wrote the paper: MT HM KI.

FULL PAPER

BJC

British Journal of Cancer (2013) 108, 932–940 | doi: 10.1038/bjc.2013.30

Keywords: circulating microRNA; biomarker; diffuse-type gastric cancer

Circulating microRNAs as biomarkers for early detection of diffuse-type gastric cancer using a mouse model

P Rotkrua[1,3,4], S Shimada[1,3], K Mogushi[2], Y Akiyama[1], H Tanaka[2] and Y Yuasa*[,1]

[1]Division of Molecular Oncology, Graduate School of Medical and Dental Sciences, Tokyo Medical and Dental University, 1-5-45 Yushima, Bunkyo-ku, Tokyo 113-8519, Japan and [2]Division of Systems Biology, Graduate School of Biomedical Science, Tokyo Medical and Dental University, 1-5-45 Yushima, Bunkyo-ku, Tokyo 113-8519, Japan

Background: Diffuse-type gastric cancer (DGC) exhibits rapid disease progression and a poor prognosis. There are no effective serum biomarkers for early detection of DGC. We have established an E-cadherin/p53 double conditional knockout (DCKO) mouse line that recapitulates human DGC morphologically and molecularly. In this study we tried to identify circulating microRNAs (miRNAs) as non-invasive biomarkers for DGC diagnosis using DCKO mice.

Methods: We performed miRNA microarray and quantitative reverse transcription–PCR analyses of tissue and serum samples from DCKO mice with DGC and age-matched littermate controls.

Results: Comparative analyses showed that mouse and human primary gastric cancers have similar miRNA expression patterns. Next, we selected some candidate miRNAs highly expressed in sera and cancer tissues of DCKO mice for further evaluation. TaqMan quantitative RT–PCR analyses indicated that four of them, miR-103, miR-107, miR-194 and miR-210, were significantly upregulated in sera of both early and advanced-stage DGC-bearing mice compared with in corresponding controls. Receiver-operating characteristic curve analyses demonstrated that these four miRNAs can discriminate DGC-positive cases from normal ones with high sensitivity and specificity.

Conclusion: These observations suggest that this mouse model of DGC is useful for identifying serum biomarkers, and we found circulating miRNAs that can accurately detect DGC at an early stage.

Gastric cancer (GC) is the fourth most common cancer and the second leading cause of cancer death worldwide (Ferlay *et al*, 2010). Gastric cancer can be classified into two major subtypes: intestinal-type GC (IGC) and diffuse-type GC (DGC) (Laurén, 1965; Japanese Gastric Cancer Association, 1998; Yuasa, 2003). Diagnosis of GC is frequently missed or delayed because there are no symptoms or signs in early stages of the disease. Although endoscopic and microscopic examinations exhibit high reliability for early detection of GC, they are invasive and inappropriate for routine screening. Routine clinical application requires easily implementable tests for biomarker analyses. Some markers in serum such as CEA and CA19-9 are not sensitive or specific enough (Liu *et al*, 2011). Thus, the best way to use serum tumour markers for diagnosing GC has not been found.

MicroRNAs (miRNAs), which are non-coding RNAs of ~22 nucleotides in length, inhibit gene expression at the post-transcriptional level, and have crucial roles in a broad range of physiological and pathological processes. MicroRNAs are

*Correspondence: Dr Y Yuasa; E-mail: yuasa.monc@tmd.ac.jp
[3]These authors contributed equally to this work.
[4]Present address: Department of Preclinical Science (Biochemistry), Faculty of Medicine, Thammasat University, Klong Luang, Pathumthani 12121, Thailand.

Received 31 October 2012; revised 21 December 2012; accepted 7 January 2013; published online 5 February 2013

estimated to regulate the expression of >60% of human protein-coding genes. Surprisingly, miRNAs show unexpected stability in serum. There are at least three proposed mechanisms underlying how miRNAs are released and protected in the bloodstream. The delivery of miRNAs is mediated by exosome and microvesicle (Valadi *et al*, 2007), Argonaute2 (Ago2) (Arroyo *et al*, 2011), and high-density lipoprotein (Vickers *et al*, 2011). Several lines of evidence have demonstrated that circulating miRNAs exhibit unique profiles for each tumour and histopathological subtype (Cortez *et al*, 2011; Song and Meltzer, 2012). Therefore, the discovery of miRNAs in serum opens up the possibility of novel biomarkers for non-invasive diagnostic screening.

Even though some circulating miRNAs have recently been identified as potential biomarkers for several types of cancers including GC, the results were inconsistent among studies. This might be due to differences in the histopathological subtypes of the study subjects, or the lack of standardised sample collection and storage methods. The utilisation of genetically engineered mouse models could minimise these problems because we can control the age of the mice, the stage of the tumours, homogeneous breeding, environmental factors, the health conditions and the sampling protocol (Kuick *et al*, 2007). We have established an E-cadherin/p53 double conditional knockout (DCKO) mouse model that recapitulates human DGC morphologically and molecularly (Shimada *et al*, 2012). Diffuse-type gastric cancers develop from the age of 6 months in DCKO mice, and early- and advanced-stage DGCs are found in 100% and 69% of 12-month-old ones, respectively. Moreover, lymph node (LN) metastasis of DGC was observed in 40% of cancer-positive cases.

In this study, first, we demonstrated that DCKO mouse and human GCs are very similar in their miRNA expression patterns. Next, we searched for candidate DGC-specific miRNA biomarkers in sera using DCKO mice at different ages, that is, with each stage of DGC. Our results suggested that miR-103, miR-107, miR-194 and miR-210 were significantly upregulated in both DCKO mouse sera and DGC tissues compared with in control mice, and that these miRNA signatures are useful biomarkers for detecting early-stage DGC.

MATERIALS AND METHODS

Mouse tissue and serum samples. The DCKO (*Atp4b-Cre*$^{+}$; *Cdh1*$^{loxP/loxP}$;*Trp53*$^{loxP/loxP}$) mouse line was described previously (Shimada *et al*, 2012). To minimise genetic background differences, *Atp4b-Cre*$^{-}$;*Cdh1*$^{loxP/loxP}$;*Trp53*$^{loxP/loxP}$ age-matched littermates were used as controls. Tumour tissues from DCKO mice and normal tissues from control mice were dissected out, and subsequently formalin-fixed and paraffin-embedded for histological analyses. Pathological classification was performed according to the criteria established by the Japanese Gastric Cancer Association (Japanese Gastric Cancer Association, 1998) and Laurén's classification (Laurén, 1965). Whole blood was taken by cardiac puncture from mice at different ages (3, 6–12 and 12 months). The blood samples were allowed to stand at room temperature for at least 1 h to a maximum of 2 h. Mouse sera were separated from clots by centrifugation at 15 000 r.p.m. for 10 min at 4 °C, and stored at −80 °C. All animal experiments were conducted following the protocols approved by the Institutional Animal Care and Use Committee of Tokyo Medical and Dental University.

Microarray profiling of tissue and serum miRNAs. Total RNA was extracted from primary GC and LN metastases of three DCKO mice, and normal stomach and LN of three age-matched littermates with TRIzol reagent (Invitrogen, Carlsbad, CA, USA). MicroRNA microarray analyses were carried out by an outsource research company, Toray Industries, Inc. (Kanagawa, Japan). MicroRNA microarray profiling was performed on Mouse miRNA Oligo chip ver.16. The nucleotides on the chip can detect ~1100 types of mouse miRNAs selected from database miRBase (http://www.mirbase.org/) release 16.0.

To assess contamination by normal tissues of tumour samples, we performed single-stranded cDNA synthesis using SuperScript III reverse transcriptase (Invitrogen) and RT–PCR with the primer sets shown in Supplementary Table S1. As mentioned in our previous report (Shimada *et al*, 2012), *Fibronectin 1 (Fn1)* and *Atp4a* are good markers for distinguishing GC from normal gastric mucosae in DCKO mice (Supplementary Figure S1A). *Mucin 1 (Muc1)* and *Cd8a* are tissue-specific markers of GC and normal LN, respectively, (Supplementary Figure S1B). Transcripts of *Gapdh*, glyceraldehyde-3-phosphate dehydrogenase, and *Hmbs*, a house keeping gene coding porphobilinogen deaminase, were amplified as internal controls.

One hundred microliters of each serum sample from five DCKO mice (12 months old) and five age-matched control mice were pooled to give a final volume of 500 µl. MicroRNA was extracted from the pooled sera based on Toray's original protocol. RNA quality and concentration were assessed by this company using an Agilent 2100 Bioanalyzer and a spectrophotometer (Agilent Technologies, Palo Alto, CA, USA). MicroRNA microarraying of each pooled sample was performed by the same method as that described above.

RNA isolation from serum samples. One hundred microliters of serum was thawed on ice and then transferred to a tube containing 150 µl of nuclease-free water. The samples were each added to 750 µl of TRIzol LS reagent (Invitrogen), followed by homogenisation by pipetting up and down several times. To allow for normalisation of sample-to-sample variation, 25 fmol of synthetic *C. elegans* miRNA cel-miR-39 (5 µl of 5 nM miRNA mimic) (Qiagen, Hilden, Germany) was added to the denatured samples. Total RNA in serum samples was then extracted according to the manufacturer's protocol.

Real-time quantitative RT- PCR (qRT–PCR) of miRNAs. The levels of miRNAs in serum samples were determined using TaqMan MicroRNA Assays (Applied Biosystems, Foster City, CA, USA). TaqMan miRNA reverse transcription was performed with miRNA-specific stem-loop primers. The amplification was carried out by denaturation at 95 °C for 10 min, followed by 45 cycles of 95 °C for 15 s and 58 °C for 60 s. Each reaction was performed in triplicate. Spiked-in cel-miR-39 was analysed as a normalisation control and relative expression was calculated using the $2^{-\Delta\Delta Ct}$ method (Livak and Schmittgen, 2001).

Statistical analysis. R statistical software (R Foundation for Statistical Computing, Vienna, Austria) was utilised to calculate correlation coefficients in regression analyses. Fisher's exact test, Student's *t*-test and Mann–Whitney *U*-test were also performed using R. Statistical significance was defined as $P<0.05$. The sensitivity, specificity and cutoff value were calculated according to standard formulas. The receiver-operating characteristic (ROC) curve and area under the curve (AUC) were established to discriminate mice with and without DGC.

RESULTS

Comparison of miRNA expression profiles of mouse and human primary GC. We analysed the miRNA profiles of primary DGC in DCKO mice using Mouse miRNA Oligo chip ver.16. To compare the miRNA expression profiles of mouse and human GC, we investigated the expression levels of miRNAs that were found to be

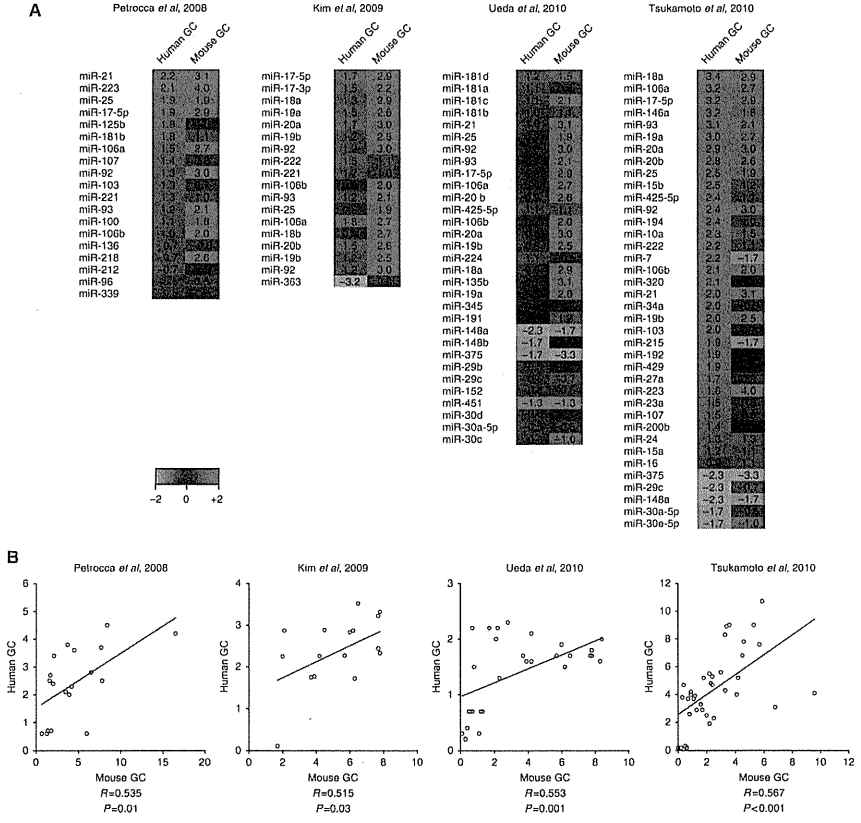

Figure 1. Heat maps (A) and dot plots (B) of miRNA expression profiles in mouse and human primary GC using homologous miRNAs reported by Petrocca *et al* (2008), Kim *et al* (2009), Ueda *et al* (2010) and Tsukamoto *et al* (2010), respectively. The expression levels of miRNAs are represented by log2 ratios and fold-changes as to normal gastric tissues from control mice or humans in heat maps and dot plots, respectively.

significantly upregulated or downregulated in human primary GC in four published studies (Petrocca *et al*, 2008; Kim *et al*, 2009; Ueda *et al*, 2010; Tsukamoto *et al*, 2010). Out of them, we selected miRNAs that were detected in Mouse miRNA Oligo chip ver.16, and visualised the miRNA expression patterns of mouse and human GC by means of heat maps (Figure 1a) and dot plots (Figure 1b). These comparative analyses demonstrated that DGC in DCKO mice was very similar to human GC in their miRNA signatures ($P=0.01$, 0.03, 0.001 and $P<0.001$, respectively).

Ueda *et al* (2010) have reported that eight and four miRNAs were overexpressed in human DGC and IGC, respectively. Notably, seven (miR-100, miR-125b, miR-199a, miR-99a, miR-143, miR-145 and miR-133a) of eight miRNAs upregulated in human DGC were highly expressed in mouse DGC, while none of four miRNAs upregulated in human IGC were ($P=0.01$; Fisher's exact test). Overall, microarray analyses of primary GC revealed that DCKO mice could recapitulate human DGC at the miRNA level.

Correlation of miRNA signatures of mouse tissue and serum samples. We analysed the miRNA characteristics of pooled sera from DCKO and control mice, primary GC and LN metastases of DCKO mice, and normal stomach and LN of control mice using miRNA microarrays. We selected 774 miRNAs that were detected in all of our microarray assays, and performed regression analyses of them (Figure 2). The correlation coefficients of miRNA expression patterns between normal gastric mucosae and primary GC, and normal LN and metastatic GC were high, that is, 0.933 and 0.926, respectively (Figure 2a), indicating that the differences between normal and cancer tissues are small. The correlation coefficient between primary and metastatic GC in miRNA profile, 0.973, was higher than the other two coefficients ($P<0.001$ for both; Student's *t*-test), suggesting that primary and metastatic GC exhibit similar characteristics as to miRNA expression.

Figure 2b shows that the miRNA patterns in sera were not closely associated with those in gastric tissue samples in DCKO

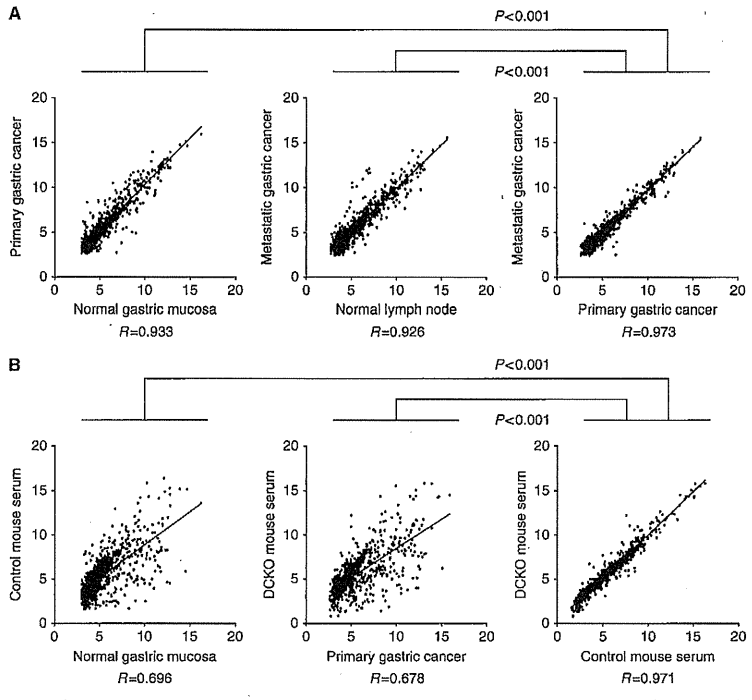

Figure 2. Dot plots of miRNA signatures in mouse normal and cancer tissue specimens (A), and in mouse tissue and serum samples (B).

mice or littermate controls ($R=0.678$ and 0.696, respectively). Sera of cancer-positive and -negative mice exhibited higher miRNA expression similarity ($R=0.971$) than pairs of tissue and serum samples in the two groups of mice ($P<0.001$ for both; Student's *t*-test), indicating that only some miRNAs overexpressed in cancer tissues could be released into the serum.

Identification of DGC-related miRNAs in sera using microarrays. We employed a strategy including screening by means of miRNA microarrays using pooled samples and validation by TaqMan qRT–PCR for individual mouse samples at different ages (Figure 3a). We initially searched for candidate miRNAs by comparing the miRNA profiles of DCKO and control mice in three types of samples: (1) DCKO *vs* control mouse sera, (2) primary DGC *vs* normal stomach tissues and (3) metastatic DGC *vs* normal stomach tissues. As shown in Figure 3b and Supplementary Table S2, the microarray analyses revealed 27 upregulated miRNAs in the sera and GC of DCKO mice compared with in controls, of which 18 were increased in LN metastasis specimens as well. In addition, 75 miRNAs that were significantly upregulated only in the sera were also identified. We selected candidate miRNAs that satisfied three criteria: (1) the level in DCKO mouse serum was >1.5-fold higher than that in controls; (2) the global normalisation value was >100 in DCKO mouse serum, indicating easily detectable levels of miRNAs; and (3) the identified miRNAs were coincidently upregulated in both sera and DGC tissues.

Candidate miRNA selection. Among the 27 and 75 candidate miRNAs identified on microarray analyses, 5 were selected for further validation based on previous papers, in which these miRNAs were reported to have important functions in carcinogenesis. We chose miR-103 and miR-107, which belong to the same family, because these two miRNAs were simultaneously upregulated in both sera and DGC tissues, but not significantly in LN metastasis tissues. The higher expression of the miR-103/107 family has been reported not only in GC (Tsukamoto *et al*, 2010) but also in other cancers such as pancreatic (Roldo *et al*, 2006), breast (Martello *et al*, 2010) and prostate (Lodes *et al*, 2009) cancers. In addition, miR-194 and miR-210 were selected from the group of miRNAs increased in sera, DGC and LN metastasis tissues. The miR-194 level was considerably high in sera (6.3-fold) and LN metastases (1.8-fold). MiR-210 has been suggested to be a serum biomarker for diffuse large B-cell lymphoma and pancreatic cancer (Cortez *et al*, 2011).

Interestingly, five members of the miR-290-295 cluster, miR-291b-5p, miR-291a-5p, miR-290-5p, miR-294* and miR-292-5p, exhibited 5.54-, 4.81-, 3.26-, 2.52- and 1.56-fold higher expression levels in DCKO mouse sera, respectively. The miR-290-295 cluster codes a family of miRNAs that was identified as cell-cycle controllers via targeting of the cell-cycle regulator genes, *Wee1* and *Fbxl5* (Lichner *et al*, 2011). A redundancy of this miRNA family in diseased mouse sera may reflect their critical functions and ability to serve as serum biomarkers. Thus, we

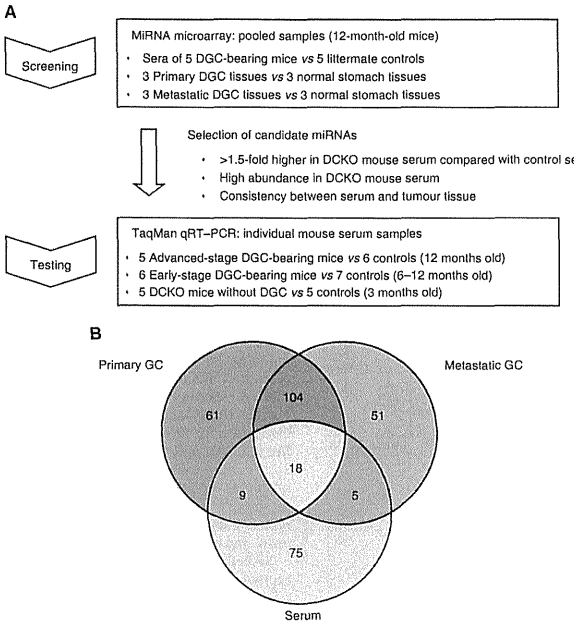

Figure 3. (A) Overview of miRNA analyses of DCKO mouse tissue and serum samples. (B) The three-way Venn diagram showing the numbers of upregulated miRNAs in DCKO mouse samples overlapping in sera, DGC tissues and lymphatic metastasis tissues.

picked miR-291b-5p as a representative for this cluster for the next validation. Totally, we selected five miRNAs, that is, miR-103, miR-107, miR-194, miR-210 and miR-291b-5p, as candidate biomarkers.

Validation of serum miRNAs by qRT–PCR in mice at different cancer stages. To evaluate the accuracy of microarray data, the levels of the five selected miRNAs in serum samples were individually assessed by TaqMan qRT–PCR. First, we examined the miRNA levels in 12-month-old DCKO mice with advanced-stage DGC ($n=5$) and age-matched controls ($n=6$) (Figure 4a). Four of the five miRNAs, miR-103, miR-107, miR-194 and miR-210, showed significant elevation in DCKO mouse sera at $P=0.045$, 0.004, 0.004 and 0.030, respectively (Mann–Whitney U-test). These results indicate that the microarray analysis data were mostly reliable. Secondly, these five miRNAs were further quantified in 6–12-month-old DCKO mice with histologically proven intramucosal DGC ($n=6$) and age-matched littermates ($n=7$) (Figure 4b). Similar to the results for mice with advanced DGC, the levels of miR-103, miR-107, miR-194 and miR-210 were significantly increased in DCKO mouse sera ($P=0.014$, 0.022, 0.014 and 0.022, respectively), suggesting the potential of these four miRNAs for identifying DGC at an early stage.

It was questionable whether upregulation of miR-103, miR-107, miR-194 and miR-210 in mice with early- and advanced-stage DGC resulted from inactivation of E-cadherin and p53 in the cells-of-origin, or was induced by the process of malignant transformation. We thus investigated whether or not the levels of the candidate miRNAs were changed in mice at 3 months of age ($n=5$), in which DGC had not been detected. As shown in Figure 4c, no significant elevation of any miRNA, miR-103, miR-107, miR-194, miR-210 or miR-291b-5p, was found in DCKO mouse sera ($P=0.421$, 0.690, 0.548, 0.548 and 0.151, respectively). This evidence suggested that upregulation of miR-103, miR-107, miR-194 and miR-210 in mice with early- and advanced-stage DGC was triggered by aberrant processes during the cancer development.

Profiles of serum miRNA levels during DGC development. The levels of the four miRNAs were examined in DCKO mice at different time points during DGC progression. The medians of their levels in both DCKO and control mouse sera were plotted at 3 months of age (no DGC), 6–12 months of age (early-stage DGC), and 12 months of age (advanced-stage DGC). Understanding the trend of candidate miRNA levels could provide an insight as to biomarker determination. Ideal biomarkers would not only be able to discriminate DGC patients from healthy ones, but also indicate the clinical stage. As shown in Figure 5, the levels of miR-103, miR-107 and miR-194 in control mouse sera were relatively constant, but not that of miR-210, whose level was significantly reduced in 12-month-old mice ($P=0.045$). On the other hand, upregulation of the miR-103 and miR-194 levels in DCKO mouse sera occurred in a stepwise manner during the progression from normal to early-stage DGC and finally to advanced-stage DGC, suggesting both of them are very suitable biomarkers for DGC diagnosis.

Although the level of miR-107 in DCKO mouse sera was slightly decreased at the advanced stage, its level was still significantly higher than that in the no DGC group ($P=0.008$). Therefore, miR-107 could be a biomarker of choice for differentiating DGC-bearing mice from normal ones. However, the level of

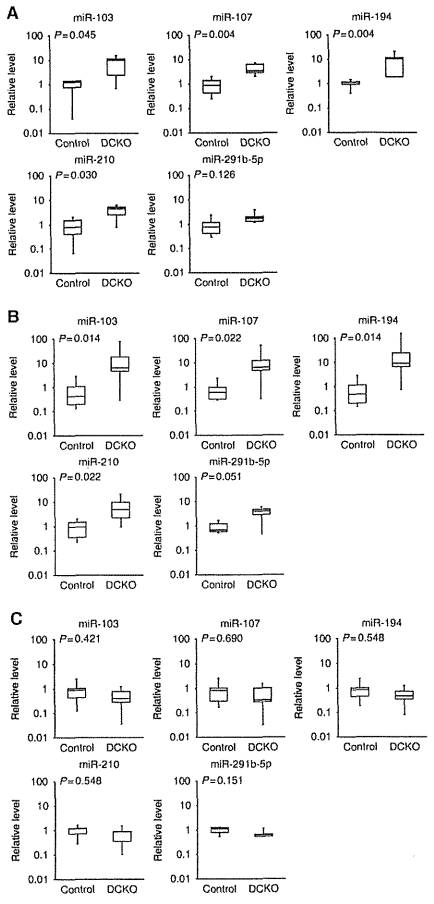

Figure 4. (A) Comparison of serum miRNA levels between DCKO ($n=5$) and control ($n=6$) mice at 12 months of age. All DCKO mice had developed advanced-stage DGC. (B) Comparison of serum miRNA levels between DCKO mice with early-stage DGC ($n=6$) and control mice ($n=7$) at 6–12 months of age. (C) Comparison of serum miRNA levels between DCKO ($n=5$) and control ($n=5$) mice at 3 months of age. Double conditional knockout mice had not developed GC yet at this age. The levels of miRNAs in all the samples were determined by qRT–PCR analyses.

miR-210 did not show a significant difference between 12-month-old DCKO mice with advanced-stage DGC and 3-month-old DCKO mice without cancer, leading to the idea that miR-210 may be an improper indicator if DGC is already advanced.

Risk assessment of candidate miRNAs in discriminating DGC from non-cancer cases. An ROC curve was plotted to identify cutoff values for miR-103, miR-107, miR-194 and miR-210 that could be used to distinguish DGC-positive cases from healthy controls (Figure 6). ROC curve analyses showed that at the cutoff level of 2.58, miR-103 exhibited 81.8% sensitivity and 95.7% specificity with an AUC of 0.881. At the cutoff level of 2.11, miR-107 exhibited 90.9% sensitivity and 95.7% specificity with an AUC of 0.909. At the cutoff level of 3.36, miR-194 exhibited 90.9% sensitivity and 95.7% specificity with an AUC of 0.925. At the cutoff level of 2.29, miR-210 exhibited 72.7% sensitivity and 87.0% specificity with an AUC of 0.846.

DISCUSSION

A mouse model of human cancer could be an efficient means of discovering diagnostic markers not only because the genetic alterations associated with human tumours can be engineered in mice, but also because mouse and human cancers can exhibit similar molecular signatures. We demonstrated that primary GC and LN metastases induced in DCKO mice resembled human GC in their miRNA expression profiles. We used this animal model of DGC to identify the circulating miRNAs that can serve as non-invasive biomarkers for DGC diagnosis. As a result of microarray analyses, five miRNAs, miR-103, miR-107, miR-194, miR-210 and miR-291b-5p, that were increased in sera from DCKO mice with DGC, were selected as candidate biomarkers. We validated that the levels of four of these five circulating miRNAs, that is, miR-103, miR-107, miR-194 and miR-210, were upregulated in sera of mice with both early- and advanced-stage DGC compared with in controls.

Several studies have revealed subsets of miRNAs whose expression levels are upregulated or downregulated in human GC (Petrocca *et al*, 2008; Kim *et al*, 2009; Tsukamoto *et al*, 2010; Ueda *et al*, 2010). They exhibited similar miRNA signatures, such as overexpression of miR-21, miR-17-92 and miR-106b-25 clusters, consistent with our finding that these miRNAs were highly expressed in primary DGC of DCKO mice on microarray analyses. In contrast, although other research groups have identified some miRNAs differentially expressed in sera or plasma of human GC patients as biomarkers, there has been a conflict as to their levels in those studies (Tsujiura *et al*, 2010; Liu *et al*, 2011; Konishi *et al*, 2012; Liu *et al*, 2012; Song *et al*, 2012). So far, no overlap of miRNA biomarkers for GC detection has been reported. The inconsistency of these results could be explained by many factors, particularly variations in histopathological types and experimental methods. The GC samples used in previous studies comprised combination of both histological subtypes (intestinal- and diffuse-types).

On the other hand, our study only involved DGC-associated samples, leading to the difference in discovered miRNAs compared with those in human GC samples. However, we found that five miRNAs had the corresponding probes in our mouse miRNA microarray data among the 11 upregulated circulating miRNAs in human GC cases reported by Liu *et al* (2012), and that four (miR-150*, miR-371-5p, miR-187* and miR-378) of these five miRNAs showed similar upregulation in sera of DCKO mice. These results suggest that the changes in serum miRNA levels in DCKO mice could be comparable to those in human GC patients.

Furthermore, there has been another study discovering miRNA biomarkers using a mouse model of prostate cancer (Selth *et al*, 2012). They performed comprehensive and quantitative analyses of serum miRNAs of the transgenic mice in the same manner as we did in this work, and have demonstrated that some serum miRNAs identified in diseased mice are shared between human and mouse prostate cancers. Therefore, although further validation with a large cohort of human samples and a prospective study are required, four miRNAs identified in this study, miR-103, miR-107,

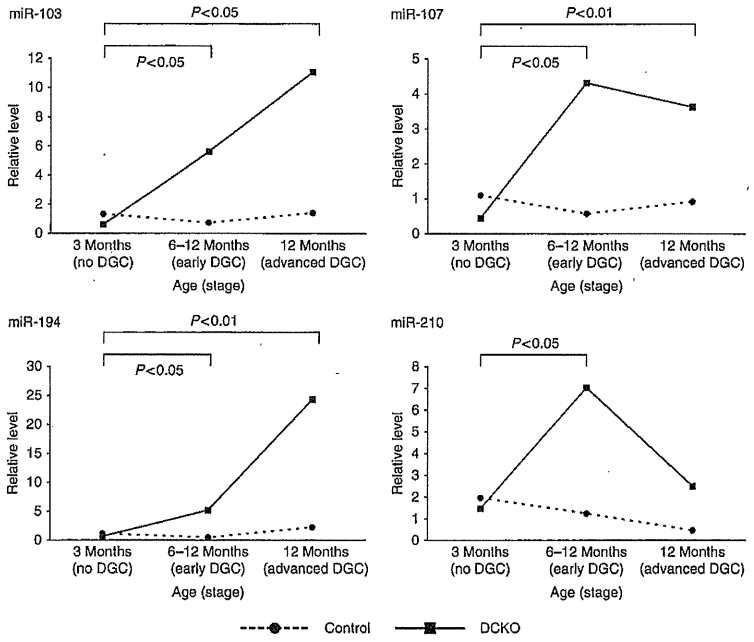

Figure 5. Time course of serum miRNA levels during DGC development. The medians of the relative levels of miR-103, miR-107, miR-194 and miR-210 in DCKO mouse sera were plotted at 3 (without DGC), 6–12 (with early-stage DGC) and 12 months of age (with advanced-stage DGC). The shape of the line shows the expression trend of the miRNAs during DGC progression.

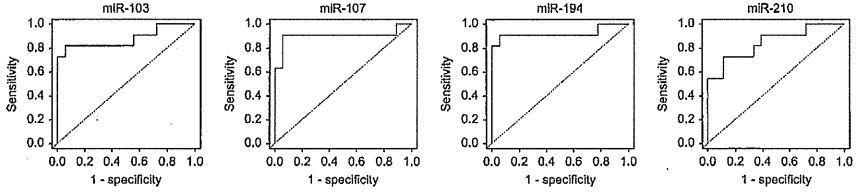

Figure 6. Receiver-operating characteristic curve analyses of the serum miR-103, miR-107, miR-194 and miR-210 levels to discriminate mice with DGC ($n=11$; not including 3-month-old DCKO mice) from healthy ones ($n=18$).

miR-194 and miR-210, could be promising as effective serum markers for DGC diagnosis and screening.

The activation of miR-103 and miR-107 in GC is consistent with a previous study that involved human tissue samples (Tsukamoto *et al*, 2010). There is evidence that the miR-103/107 family induces the epithelial-to-mesenchymal transition (EMT) in breast cancer (Martello *et al*, 2010). Taken together with our finding that EMT could have crucial roles in diffuse-type carcinogenesis in DCKO mice (Shimada *et al*, 2012), this miRNA family might be associated with the development and/or progression of the malignancy. Further functional studies on this miRNA family to determine their interactions with tumour-suppressor genes are required.

Our data showed that the miR-194 level was upregulated in all types of samples obtained from DCKO mice with DGC, that is, serum, DGC tissues and LN metastasis tissues. In a former study, Tsukamoto *et al* (2010) demonstrated that the elevation of miR-194 was as high as 5.16-fold in human GC tissues. Moreover, miR-194 has been reported to be overexpressed in oesophageal cancer (Song and Meltzer, 2012), and to be involved in the carcinogenesis in pancreatic ductal adenocarcinomas (Mees *et al*, 2010). It has been proved that miR-194 regulates metastasis formation through targeting of the metastasis-suppressor gene, *EP300* (Mees *et al*, 2010). However, the oncogenic role of miR-194 in DGC metastasis has not been determined.

In addition to for DGC, a high level of miR-210 has been supposed to be a diagnostic biomarker for other malignancies, that is, diffuse large B-cell lymphoma (Lawrie *et al*, 2008) and pancreatic cancer (Wang *et al*, 2009; Ho *et al*, 2010), and a prognostic marker for breast cancer (Camps *et al*, 2008). Two reports have mentioned that miR-210 was directly regulated by HIF1A and therefore induced by hypoxia, a common feature of solid tumours (Crosby *et al*, 2009; Mathew and Simon, 2009). Although the miR-210 level in DCKO mouse sera with advanced-stage DGC was not significantly different from that in DCKO mice without cancer, comparison of 12-month- and 3-month-old control mice also showed the similar trend that the miR-210 level had significantly decreased by 12 months of age ($P=0.045$). This reduction in the miR-210 level in 12-month-old mice for both DCKO and control mice might be dependent on age.

In summary, we have demonstrated that a mouse model of human GC provided helpful materials for discovering circulating miRNAs relevant to the clinical stage of DGC. We found that four miRNAs, miR-103, miR-107, miR-194 and miR-210, were specifically upregulated in DGC-positive mouse sera, and suggested they are novel non-invasive biomarkers for the early detection of DGC. Furthermore, the elevation of miR-103 and miR-194 occurred during the entire progression from the non-cancer status to the advanced-stage, implying their ability as biomarkers that can be used to determine the DGC stage.

ACKNOWLEDGEMENTS

This study was supported by a Grant-in-Aid for Scientific Research (B), No. 2330342, and by the A3 Foresight Program from JSPS.

CONFLICT OF INTEREST

The authors declare no conflict of interest.

REFERENCES

Arroyo JD, Chevillet JR, Kroh EM, Ruf IK, Pritchard CC, Gibson DF, Mitchell PS, Bennett CF, Pogosova-Agadjanyan EL, Stirewalt DL, Tait JF, Tewari M (2011) Argonaute2 complexes carry a population of circulating microRNAs independent of vesicles in human plasma. *Proc Natl Acad Sci USA* **108**: 5003–5008.

Camps C, Buffa FM, Colella S, Moore J, Sotiriou C, Sheldon H, Harris AL, Gleadle JM, Ragoussis J (2008) hsa-miR-210 is induced by hypoxia and is an independent prognostic factor in breast cancer. *Clin Cancer Res* **14**: 1340–1348.

Cortez MA, Bueso-Ramos C, Ferdin J, Lopez-Berestein G, Sood AK, Calin GA (2011) MicroRNAs in body fluids–the mix of hormones and biomarkers. *Nat Rev Clin Oncol* **8**: 467–477.

Crosby ME, Kulshreshtha R, Ivan M, Glazer PM (2009) MicroRNA regulation of DNA repair gene expression in hypoxic stress. *Cancer Res* **69**: 1221–1229.

Ferlay J, Shin HR, Bray F, Forman D, Mathers C, Parkin DM (2010) Estimates of worldwide burden of cancer in 2008: GLOBOCAN 2008. *Int J Cancer* **127**: 2893–2917.

Ho AS, Huang X, Cao H, Christman-Skieller C, Bennewith K, Le QT, Koong AC (2010) Circulating miR-210 as a novel hypoxia marker in pancreatic cancer. *Transl Oncol* **3**: 109–113.

Japanese Gastric Cancer Association (1998) Japanese Classification of Gastric Carcinoma – 2nd English Edition. *Gastric Cancer* **1**: 10–24.

Kim YK, Yu J, Han TS, Park SY, Namkoong B, Kim DH, Hur K, Yoo MW, Lee HJ, Yang HK, Kim VN (2009) Functional links between clustered microRNAs: suppression of cell-cycle inhibitors by microRNA clusters in gastric cancer. *Nucleic Acids Res* **37**: 1672–1681.

Konishi H, Ichikawa D, Komatsu S, Shiozaki A, Tsujiura M, Takeshita H, Morimura R, Nagata H, Arita T, Kawaguchi T, Hirashima S, Fujiwara H, Okamoto K, Otsuji E (2012) Detection of gastric cancer-associated microRNAs on microRNA microarray comparing pre- and post-operative plasma. *Br J Cancer* **106**: 740–747.

Kuick R, Misek DE, Monsma DJ, Webb CP, Wang H, Peterson KJ, Pisano M, Omenn GS, Hanash SM (2007) Discovery of cancer biomarkers through the use of mouse models. *Cancer Lett* **249**: 40–48.

Laurén P (1965) The two histological main types of gastric carcinoma: diffuse and so-called intestinal-type carcinoma. An attempt at a histo-clinical classification. *Acta Pathol Microbiol Scand* **64**: 31–49.

Lawrie CH, Gal S, Dunlop HM, Pushkaran B, Liggins AP, Pulford K, Banham AH, Pezzella F, Boultwood J, Wainscoat JS, Hatton CS, Harris AL (2008) Detection of elevated levels of tumour-associated microRNAs in serum of patients with diffuse large B-cell lymphoma. *Br J Haematol* **141**: 672–675.

Lichner Z, Páll E, Kerekes A, Pállinger E, Maraghechi P, Bosze Z, Gócza E (2011) The miR-290-295 cluster promotes pluripotency maintenance by regulating cell cycle phase distribution in mouse embryonic stem cells. *Differentiation* **81**: 11–24.

Liu H, Zhu L, Liu B, Yang L, Meng X, Zhang W, Ma Y, Xiao H (2012) Genome-wide microRNA profiles identify miR-378 as a serum biomarker for early detection of gastric cancer. *Cancer Lett* **316**: 196–203.

Liu R, Zhang C, Hu Z, Li G, Wang C, Yang C, Huang D, Chen X, Zhang H, Zhuang R, Deng T, Liu H, Yin J, Wang S, Zen K, Ba Y, Zhang CY (2011) A five-microRNA signature identified from genome-wide serum microRNA expression profiling serves as a fingerprint for gastric cancer diagnosis. *Eur J Cancer* **47**: 784–791.

Livak KJ, Schmittgen TD (2001) Analysis of relative gene expression data using real-time quantitative PCR and the 2(-Delta Delta C(T)) Method. *Methods* **25**: 402–408.

Lodes MJ, Caraballo M, Suciu D, Munro S, Kumar A, Anderson B (2009) Detection of cancer with serum miRNAs on an oligonucleotide microarray. *PLoS One* **4**: e6229.

Martello G, Rosato A, Ferrari F, Manfrin A, Cordenonsi M, Dupont S, Enzo E, Guzzardo V, Rondina M, Spruce T, Parenti AR, Daidone MG, Bicciato S, Piccolo S (2010) A microRNA targeting dicer for metastasis control. *Cell* **141**: 1195–1207.

Mathew LK, Simon MC (2009) mir-210: a sensor for hypoxic stress during tumorigenesis. *Mol Cell* **35**: 737–738.

Mees ST, Mardin WA, Wendel C, Baeumer N, Willscher E, Senninger N, Schleicher C, Colombo-Benkmann M, Haier J (2010) EP300–a miRNA-regulated metastasis suppressor gene in ductal adenocarcinomas of the pancreas. *Int J Cancer* **126**: 114–124.

Petrocca F, Visone R, Onelli MR, Shah MH, Nicoloso MS, de Martino I, Iliopoulos D, Pilozzi E, Liu CG, Negrini M, Cavazzini L, Volinia S, Alder H, Ruco LP, Baldassarre G, Croce CM, Vecchione A (2008) E2F1-regulated microRNAs impair TGFbeta-dependent cell-cycle arrest and apoptosis in gastric cancer. *Cancer Cell* **13**: 272–286.

Roldo C, Missiaglia E, Hagan JP, Falconi M, Capelli P, Bersani S, Calin GA, Volinia S, Liu CG, Scarpa A, Croce CM (2006) MicroRNA expression abnormalities in pancreatic endocrine and acinar tumors are associated with distinctive pathologic features and clinical behavior. *J Clin Oncol* **24**: 4677–4684.

Selth LA, Townley S, Gillis JL, Ochnik AM, Murti K, Macfarlane RJ, Chi KN, Marshall VR, Tilley WD, Butler LM (2012) Discovery of circulating microRNAs associated with human prostate cancer using a mouse model of disease. *Int J Cancer* **131**: 652–661.

Shimada S, Mimata A, Sekine M, Mogushi K, Akiyama Y, Fukamachi H, Jonkers J, Tanaka H, Eishi Y, Yuasa Y (2012) Synergistic tumour suppressor activity of E-cadherin and p53 in a conditional mouse model for metastatic diffuse-type gastric cancer. *Gut* **61**: 344–353.

Song JH, Meltzer SJ (2012) MicroRNAs in pathogenesis, diagnosis, and treatment of gastroesophageal cancers. *Gastroenterology* **143**: 35–47.

Song MY, Pan KF, Su HJ, Zhang L, Ma JL, Li JY, Yuasa Y, Kang D, Kim YS, You WC (2012) Identification of serum microRNAs as novel non-invasive biomarkers for early detection of gastric cancer. *PLoS One* **7**: e33608.

Tsujiura M, Ichikawa D, Komatsu S, Shiozaki A, Takeshita H, Kosuga T, Konishi H, Morimura R, Deguchi K, Fujiwara H, Okamoto K, Otsuji E (2010) Circulating microRNAs in plasma of patients with gastric cancers. *Br J Cancer* **102**: 1174–1179.

Tsukamoto Y, Nakada C, Noguchi T, Tanigawa M, Nguyen LT, Uchida T, Hijiya N, Matsuura K, Fujioka T, Seto M, Moriyama M (2010)

MicroRNA-375 is downregulated in gastric carcinomas and regulates cell survival by targeting PDK1 and 14-3-3zeta. *Cancer Res* 70: 2339–2349.

Ueda T, Volinia S, Okumura H, Shimizu M, Taccioli C, Rossi S, Alder H, Liu CG, Oue N, Yasui W, Yoshida K, Sasaki H, Nomura S, Seto Y, Kaminishi M, Calin GA, Croce CM (2010) Relation between microRNA expression and progression and prognosis of gastric cancer: a microRNA expression analysis. *Lancet Oncol* **11**: 136–146.

Valadi H, Ekström K, Bossios A, Sjöstrand M, Lee JJ, Lötvall JO (2007) Exosome-mediated transfer of mRNAs and microRNAs is a novel mechanism of genetic exchange between cells. *Nat Cell Biol* 9: 654–659.

Vickers KC, Palmisano BT, Shoucri BM, Shamburek RD, Remaley AT (2011) MicroRNAs are transported in plasma and delivered to recipient cells by high-density lipoproteins. *Nat Cell Biol* 13: 423–433.

Wang J, Chen J, Chang P, LeBlanc A, Li D, Abbruzzese JL, Frazier ML, Killary AM, Sen S (2009) MicroRNAs in plasma of pancreatic ductal adenocarcinoma patients as novel blood-based biomarkers of disease. *Cancer Prev Res* 2: 807–813.

Yuasa Y (2003) Control of gut differentiation and intestinal-type gastric carcinogenesis. *Nat Rev Cancer* 3: 592–600.

Supplementary Information accompanies this paper on British Journal of Cancer website (http://www.nature.com/bjc)

HEPATOLOGY
Official Journal of the American Association for the Study of Liver Diseases

Contrast-Enhanced Intraoperative Ultrasonography for Vascular Imaging of Hepatocellular Carcinoma: Clinical and Biological Significance

Kota Sato,[1] Shinji Tanaka,[1] Yusuke Mitsunori,[1] Kaoru Mogushi,[2] Mahmut Yasen,[1] Arihiro Aihara,[1] Daisuke Ban,[1] Takanori Ochiai,[1] Takumi Irie,[1] Atsushi Kudo,[1] Noriaki Nakamura,[1] Hiroshi Tanaka,[2] and Shigeki Arii[1]

Abnormal tumor vascularity is one of the typical features of hepatocellular carcinoma (HCC). In this study, the significance of contrast-enhanced intraoperative ultrasonography (CEIOUS) images of HCC vasculature was evaluated by clinicopathological and gene expression analyses. We enrolled 82 patients who underwent curative hepatic resection for HCC with CEIOUS. Clinicopathological and gene expression analyses were performed according to CEIOUS vasculature patterns. CEIOUS images of HCC vasculatures were classified as reticular HCC or thunderbolt HCC. Thunderbolt HCC was significantly correlated with higher alpha-fetoprotein levels, tumor size, histological differentiation, portal vein invasion, and tumor-node-metastasis stage, and these patients demonstrated a significantly poorer prognosis for both recurrence-free survival ($P = 0.0193$) and overall survival ($P = 0.0362$) compared with patients who had reticular HCC. Gene expression analysis revealed that a rereplication inhibitor geminin was significantly overexpressed in thunderbolt HCCs ($P = 0.00326$). *In vitro* knockdown of geminin gene reduced significantly the proliferation of human HCC cells. Immunohistochemical analysis confirmed overexpression of geminin protein in thunderbolt HCC ($P < 0.0001$). Multivariate analysis revealed geminin expression to be an independent factor in predicting poor survival in HCC patients ($P = 0.0170$). *Conclusion:* CEIOUS vascular patterns were distinctly identifiable by gene expression profiling associated with cellular proliferation of HCC and were significantly related to HCC progression and poor prognosis. These findings might be clinically useful as a determinant factor in the postoperative treatment of HCC. (HEPATOLOGY 2013;57:1436-1447)

Hepatocellular carcinoma (HCC) is the fifth most common malignancy and one of the most common causes of cancer-related death in the world.[1,2] Surgical resection is considered the primary curative therapy in the treatment of HCC.[3-5] During hepatic resection, intraoperative ultrasonography (IOUS) of the liver is used as an aid for surgical navigation. IOUS provides crucial diagnostic and staging information to the surgeon during the procedure.[6] Recently, contrast-enhanced ultrasonography techniques using microbubble agents have been developed.[7] Among these agents, Sonazoid (gaseous perflubutane; Daiichi-Sankyo, Tokyo, Japan) is a unique ultrasound contrast agent that is accumulated in Kupffer cells.[8-12] We reported recently that Kupffer imaging of Sonazoid with contrast-enhanced intraoperative ultrasonography (CEIOUS) is quite useful for detailed detection of tumors in real time during hepatic resection.[13]

Tumor angiogenesis is one of the critical features in determining overgrowth and metastatic potential.[14,15] In contrast to normal vessels, tumor vessels are tortuous, excessively branched, and short-circuited. In this manner, tumor vasculature is highly disorganized.[14-18] HCC is a tumor that is typically known to exhibit angiogenesis.[2,3,18-23] In particular, a dramatic alteration in arterial hypervascularity is observed in moderately and poorly differentiated HCC.[18,20,21] Such hypervascularity can be observed using angiography and contrast-enhanced computed tomography,[21,24,25] but it is quite difficult to analyze the detailed intratumoral vasculature in real time.

Recently, it has been reported that contrast-enhanced ultrasonography can be used to evaluate tumor vasculature similarly to what is seen with other contrast-enhanced radiological imaging techniques.[22,23,34] In the present study, the HCC vasculature was analyzed in detail by CEIOUS with Sonazoid to identify the specific patterns associated with clinicopathological features. Additionally, genome-wide gene expression was assessed via DNA microarray analysis, which offers a systematic approach to acquire comprehensive information regarding gene transcription profiles.[26] Such studies could lead not only to the identification of unique biomarkers but also to the development of a novel molecular-targeted therapy for HCC.[27-30] The present study demonstrates the evidence indicating the biological and clinical significance of CEIOUS microflow imaging (MFI).

Patients and Methods

Patients and Samples. We enrolled patients who underwent curative hepatic resection for HCC at the Tokyo Medical and Dental University Hospital between August 2007 and March 2010. From a total of 167 patients with HCC, 135 patients underwent CEIOUS of the main tumor during hepatic resection. Among them, 82 patients were technically eligible for MFI analysis. The other 53 patients were technically ineligible for MFI mainly because of pretreatment with sorafenib, radiofrequency ablation, and transcatheter arterial chemoembolization. The baseline characteristics of the enrolled patients are summarized in Table 1. Written informed consent was obtained from the patients, and the institutional review board approved the study. The preoperative evaluations have been described elsewhere.[31] Resected tissue containing no necrosis was divided into two specimens immediately after surgery: one was snap-frozen in liquid nitrogen and stored at −80°C for microarray analysis; the other was fixed in 10% formaldehyde solution and embedded in paraffin for histopathological analysis. According to *The General Rules for the Clinical and Pathological Study of Primary Liver Cancer*,[32] histopathological analysis was performed. To confirm the expression patterns detected by the microarrays, the median follow-up period was 784 days (interquartile range, 497-1,015).

Table 1. Patient Characteristics

Characteristic	Value
Age, years, *mean* ± SD (range)	70 ± 9.0 (34-84)
Sex, no., male:female	62:20
Viral infection, no., HBV:HCV:non-B/C	13:46:23
Background liver pathology, no.	
Normal	6
Chronic hepatitis or liver fibrosis	33
Liver cirrhosis	43
Child-Pugh classification, no., A:B	78:4
Albumin, mg/dL, mean ± SD	4.1 ± 0.4
Total bilirubin, mg/dL, mean ± SD	0.90 ± 0.40
PT%, mean ± SD	82.2 ± 8.0
AFP, ng/mL, *mean* ± SE	5,751 ± 4,832
PIVKA-II, mAU/mL, mean ± SE	7,355 ± 3,575
Tumor size, cm, mean ± SD	4.2 ± 3.4 (1-25)
Tumor number, no., solitary:multiple	49:33
TNM stage, I:II:III:IV	5:28:32:17

HBV, hepatitis B virus; HCV, hepatitis C virus; PIVKA-II, protein induced by vitamin K absence or antagonist II; PT%, prothrombin time.

Analysis of MFI via CEIOUS. The ultrasound system Xario-XG (Toshiba Medical) was used for all IOUS and CEIOUS procedures with a 7-MHz, T-shaped linear probe (PLT-705BTH; Toshiba Medical). CEIOUS was performed with pulse inversion harmonic imaging capability. The mechanical index was set at 0.15 in all CEIOUS procedures. The acoustic power was altered to keep the mechanical index at 0.15 because the depth of the focus point varied. During CEIOUS procedures, a real-time fundamental mode image was displayed simultaneously with a pulse inversion harmonic image side-by-side for reference. Thus, the target lesions were not missed even if they were difficult to recognize in the pulse inversion harmonic imaging. During the operation, the liver was mobilized off the diaphragm for improved sonographic visualization. IOUS was then performed in a systematic fashion in baseline fundamental mode scan to

Abbreviations: AFP, alpha-fetoprotein; CEIOUS, contrast-enhanced intraoperative ultrasonography; FC, fold change; HCC, hepatocellular carcinoma; IOUS, intraoperative ultrasonography; MFI, micro-flow imaging; PBS, phosphate-buffered saline; preRC, prereplication complex; siRNA, small interfering RNA; TNM, tumor-node-metastasis.

From the [1]Department of Hepato-Biliary-Pancreatic Surgery, Graduate School of Medicine; and the [2]Information Center for Medical Sciences, Tokyo Medical and Dental University, Tokyo, Japan.

Received April 16, 2012; accepted October 20, 2012.

Supported by a Grant-in-Aid for Scientific Research on Innovative Areas, Scientific Research (A) from the Ministry of Education, Culture, Sports, Science & Technology of Japan and a Health & Labour Sciences Research Grant from the Ministry of Health Labour & Welfare of Japan.

Address reprint requests to: Shinji Tanaka, M.D., Ph.D., F.A.C.S., Department of Hepato-Biliary-Pancreatic Surgery, Graduate School of Medicine, Tokyo Medical and Dental University, 1-5-45 Yushima, Bunkyo-ku, Tokyo 113-8519, Japan. E-mail: shinji.msrg@tmd.ac.jp; fax: (81)-3-5803-0263.

View this article online at wileyonlinelibrary.com.

DOI 10.1002/hep.26122

Potential conflict of interest: Nothing to report.

Additional Supporting Information may be found in the online version of this article.

confirm the preoperative tumor staging. There was no lesion discovered in the preoperative staging found during IOUS. After IOUS, Sonazoid was injected at a dose of 0.5 mL/body in approximately 1 second through a catheter inserted in the antecubital vein, followed by a 10-mL normal saline flush. Following injection, a dynamic CEIOUS was performed with the focus depth beyond the main tumor. The main tumor was observed continuously for approximately 1 minute from the time of injection (vascular phase). The arterial phase was timed for 45 seconds after completion of the flash, after which the portal venous phase was timed from 45 to 70 seconds after injection. We performed MFI after observation of the portal venous phase. For MFI analysis, the combination of flash replenishment sequence and the maximum intensity holding sequence was expected to make it possible to visualize the tumor vasculature clearly with high special resolution and vascular continuity.[23] The accumulation time for each MFI sequence was 10-15 seconds, depending on the perfusion of the target tissue. As the standardized procedure, we applied three-time flashes on the main tumor and confirmed the MFI pattern based on the dominant image during CEIOUS. At approximately 10-15 minutes after injection, ultrasonic observation was resumed using pulse inversion harmonic imaging in the systematic liver (Kupffer phase). Hypoechoic lesions were searched for in hyperechoic surrounding liver with accumulated microbubbles. The focus point was set at the bottom of the liver. In the case of new lesions detected, we performed defect reperfusion imaging with an additional injection of Sonazoid (0.5 mL/body). The observation in the Kupffer phase was not repeated after the second injection because all focal liver lesions were theoretically examined by a thorough scan in the first Kupffer phase. We removed all lesions diagnosed as HCC by each modality under conditions that ensured safety. The IOUS and CEIOUS scans and image analysis were performed in consensus reading by surgeons with 8, 10, 20, and 40 years of experience in liver surgery.

DNA Microarray Analysis. For the gene expression analysis, at least three sections of the largest nodule were used from the largest cross-section of the main tumor. Total RNA was extracted from the HCC specimens with an RNeasy kit (Qiagen, Hilden, Germany). The integrity of the RNA obtained was assessed with an Agilent 2100 Bioanalyzer (Agilent Technologies, Palo Alto, CA). Among the HCC tumors limited to $\leq$4 cm in diameter to exclude the bias of tumor size, 27 samples (11 reticular HCC, 16 thunderbolt HCC) were available for analysis of gene expression. In the 27 samples, the mean size of the tumor was 2.9 $\pm$ 0.2 cm. Contaminating DNA was removed by digestion with RNase-free DNase (Qiagen), and with 2 μg of total RNA, complementary RNA was prepared with a one-cycle target labeling and control reagents kit (Affeymetrix, Santa Clara, CA). The hybridization and signal detection of the Human Genome U133 (HG-U133) Plus 2.0 arrays (Affymetrix) were performed in accordance with the manufacturer's instructions. A total of 37,743 microarray data sets were normalized by the robust multiarray average method (R2.4.1 statistical software together with the BioConductor package), essentially as described in our previous report.[31] The estimated gene expression levels were log 2 transformed, and the fold change (FC) values were calculated using ratios of genometric means of gene expression levels between two MFI patterns. A Wilcoxon rank sum test was performed to estimate the significance levels of the differences in gene expression between the two groups. For each statistical test, the obtained P values from the multiple hypothetical testing were adjusted by a false discovery rate, and probe sets with a false discovery rate <0.47 were considered for further analysis. Hierarchical clustering with the selected probe sets was performed using a plete linkage method. For visualization, the expression levels were standardized as z scores (mean = 0, variance = 1) for each probe set.

Cell Culture. The human HCC cell lines SK-Hep1, Hep3B, and PLC/PRF/5 were obtained from American Type Culture Collection (Manassas, VA). The other human HCC cell lines Huh1, Huh7, HLE, HLF, and HepG2 were obtained from the Human Science Research Resources Bank (Osaka, Japan). The culture media used were Roswell Park Memorial Institute 1640 medium (SK-Hep1, Hep3B, Huh7, and HepG2) and Dulbecco's modified Eagle medium (PLC/PRF/5, Huh1, HLE, and HLF) supplemented with 5% fetal bovine serum for the HLF cells or 10% fetal bovine serum for the remaining cell lines. All media were supplemented with 100 U/mL of penicillin and 100 μg/mL of streptomycin. All cell lines were cultivated in a humidified incubator at 37°C in 5 % carbon dioxide and were collected with 0.25% trypsin-0.03% ethylene diamine tetraacetic acid.

Western Blotting and Immunocytochemistry. Geminin protein expression in the cell lines was detected via western blotting analysis. The total protein was extracted from each cell line as described.[33] The protein levels of geminin and α-tubulin (control) were detected via standard western blot analysis by using 8-15% sodium dodecyl sulfate–polyacrylamide gel electrophoresis.

The blots were incubated overnight at 4°C with the primary antibody, anti-human geminin (1:200; Santa Cruz Biotechnology, Santa Cruz, CA; catalog #sc-13015), and then at room temperature for 1 hour with anti–α-tubulin (1:5,000; Sigma-Aldrich, St.Louis, MO; catalog #T9026). The appropriate secondary antibodies were added for 2 hours, and the protein expression was visualized with enhanced chemiluminescence by the ECL western blot testing detection system (GE Healthcare, Buckinghamshire, UK). The immunocytochemical analysis was performed with cultured cells on glass slides coated with saline. The cells were fixed in phosphate-buffered saline (PBS)-10% trichloroacetic acid for 15 minutes, permeabilized in PBS-0.2% Triton X-100 for 5 minutes, and then blocked in PBS-3% bovine serum albumin for the immunocytochemical detection of geminin. The primary antibody (Santa Cruz Biotechnology) was used at 1:50 dilution, and γ-tubulin antibody (Sigma-Aldrich; catalog #T6557) was used at 1:1,000. The secondary antibody for geminin was the Alexa Fluor 568 fragment of a donkey anti-rabbit immunoglobulin G (H+L) and antibody for γ-tubulin was the Alexa Fluor 488 fragment of a donkey anti-mouse immunoglobulin G (H+L) (Invitrogen, Carsbad, CA). The DNA was counterstained with 4',6-dia-midino-2-phenylindeole. Image acquisition was performed on a confocal microscope (Axio Observer.ZL, Carl Zeiss Microimaging GmbH, Germany).

Gene Silencing. The knockdown of geminin was performed by using small interfering RNA (siRNA) (Invitrogen; catalog #1299003) and negative control siRNA duplexes (Invitrogen; catalog #12935112). HLF, SK-Hep1, and Hep3B cells were seeded at a density of 1.0×10^5 cells into 6-well plates in 2,000 μL of culture medium with 5% fetal bovine serum for the HLF cells or 10% fetal bovine serum for Hep3B and SK-Hep1 (for western blot testing, cell proliferation analysis, cell cycle analysis). Thereafter, transfection with the siRNA was performed by using Lipofectamine 2000 (Invitrogen) according to the manufacturer's instructions. After transfection, the cells were incubated for 96 hours at 37°C in a 5% carbon dioxide atmosphere. At the 0-, 24-, 48-, 72-, and 96-hour time points after siRNA transfection, cells were detached from each plate. The number of viable cells was counted by an automatic cell counting machine (CYTORECON; GE Healthcare) according to the manufacturer's instructions. The number of nonviable cells was assessed using CYTORECON and trypan blue dye exclusion. These experiments were independently evaluated in triplicate for cell proliferation analysis. And fluorescence-activated cell sorting for cell cycle analysis was done on cells that were collected by trypsinization on each point after siRNA transfection cells, fixed with 70% ethanol overnight at 4°C. Cells were rehydrated in PBS and then resuspended in PBS containing 100 μg/mL RNase (Sigma) and 10 μg/mL propidium iodide. Cellular DNA content was analyzed with a FACSCaliber flow cytometer (Becton Dickinson Biosciences, San Joes, CA) using Cellquest software.

Immunohistochemical Analysis. Immunohistochemical analysis was performed on HCC tissue samples. The primary antibodies were used at the following concentrations diluted in PBS containing 1% bovine serum albumin: geminin (1:500; Santa Cruz Biotechnology), Ki67 (1:100; Abcam, Cambridge, UK; catalog #ab833), EpCAM (1:3,000; AbD Serotec, Oxford, UK; catalog #MCA1870G), CK19 (1:100; Dako, Glostrup, Denmark; catalog #M088801), and c-KIT (Ventana XT System; Ventana, Tucson, AZ; catalog 790-2951). The tissue sections were stained by an automated immunostainer (Ventana XT System) using heat-induced epitope retrieval and a standard DAB detection kit (Ventana). The immunostaining was evaluated quantitatively by counting at least 500 cells in three different random fields (magnification ×100) under a light microscope by three independent investigators (Sato, Tanaka, and Arii). The mean value was calculated for the final result of each case.

Statistical Analysis. Statistical comparisons of clinicopathological characteristics for significance were performed using a χ^2 test or Fisher's exact test with a single degree of freedom, and a Student t test was used to analyze the differences between continuous values. Overall survival and recurrence rates were determined by the Kaplan-Meier method, and for comparisons, log-rank tests were used. P values less then 0.05 were considered to have statistical significance. To investigate those factors that predicted overall survival, multivariate analyses were performed using Cox proportional hazard models and logistic regression models. All statistical analyses were performed using SPSS version 17.0 (SPSS, Chicago, IL).

Results

Classification of MFI Patterns and Postoperative Outcomes of Patients with HCC. A total of 82 patients who underwent CEIOUS examination during hepatic resection of HCC were analyzed. According to MFI data, tumor vasculatures were classified as two characteristic patterns: a thin, ramified pattern (reticular HCC) and a thick, linear pattern (thunderbolt HCC), although such a difference could not be